PVP surfactant-modified flower-like BiOBr with tunable bandgap structure for efficient photocatalytic decontamination of pollutants

ZHANG, Bofan, ZHANG, Mutian, ZHANG, Liang, BINGHAM, Paul <http://orcid.org/0000-0001-6017-0798>, LI, Wen and KUBUKI, Shiro

---

Citation:

ZHANG, Bofan, ZHANG, Mutian, ZHANG, Liang, BINGHAM, Paul, LI, Wen and KUBUKI, Shiro (2020). PVP surfactant-modified flower-like BiOBr with tunable bandgap structure for efficient photocatalytic decontamination of pollutants. Applied Surface Science, 530. [Article]

PVP surfactant-modified flower-like BiOBr with tunable bandgap structure for efficient photocatalytic decontamination of pollutants

Bofan Zhang[1, *, †] , Mutian Zhang[2, †], Liang Zhang[3], Paul A. Bingham[4], Wen Li[2], Shiro Kubuki[1]

[1]Department of Chemistry, Tokyo Metropolitan University, 1-1 Minami-Osawa, Hachi-Oji, Tokyo 192-0397, Japan

[2]School of Material Science and Engineering, Ocean University of China, 238 Songling Road, Laoshan District, Qingdao, China

[3]Mössbauer Effect Data Center, Dalian Institute of Chemical Physics, Chinese Academy of Sciences, Dalian 116023, China

[4]College of Business, Technology and Engineering Faculty of Science, Technology and Arts, Sheffield Hallam University, Howard Street, Sheffield S1 1WB, UK

*Corresponding author:

Zhang Bofan, Tokyo Metropolitan University, Tokyo 192-0397, Japan; E-mail: 15054218031@163.com

Abstract

Designing semiconductor catalysts with superior charge carrier transfer and adequately exposed reactive sites is crucial for acquiring remarkable photocatalytic activity. Herein, a series of BiOBr catalysts with PVP as “organic armor” were synthesized via a facile precipitation strategy. As expected, the BiOBr-PVP hybrids exhibited superior catalytic oxidation toward the removal of organic dyes and tetracycline, but also catalytic reduction of Cr (VI). By virtue of tunable bandgap structure, sufficient abundance of reactive sites and decreased work function, the BiOBr-PVP composites could effectively expedite the charge carrier separation and transfer via enhanced transport pathways. Simultaneously, the reduced particle size and enlarged specific surface area achieved by loading PVP on the BiOBr catalyst could provide greater contact area and channels for intimate interaction between reactive sites and pollutants. Moreover, a photodegradation pathway for tetracycline was proposed based on LC-MS measurements and the intrinsic mechanism between BiOBr and PVP was discussed by first-principles calculation. The constructed BiOBr-PVP composites extend the scope and comprehension of photocatalysts via surface structural engineering and sufficient interfacial coupling for use in several environmental purification applications.

Keywords: Photocatalysis, BiOBr, Bandgap structure, Interfacial coupling, Degradation pathway.

1. Introduction

In recent decades, water pollution associated with antibiotics, industrial dyes and heavy metals has been attracted much concern, due to serious negative impacts on the environment and human development [1, 2]. Lately, various technologies and strategies have been applied to purify and thereby selectively remove these contaminants. These include adsorption [3, 4], Fenton oxidation, microwave catalysis [5, 6] and photocatalysis [7-9]. Among these methods, semiconductor photocatalysis has been considered to be an efficient and environmentally-friendly technology due to its mild reaction conditions [10-12], high catalytic efficiency and convenient operation [13-15]. Unfortunately, the limited solar absorption range, lower quantum efficiency, and limited UV light-response hinder its application more widely in practical wastewater treatment [16]. Therefore, it is desirable to explore higher catalytic activity and more efficient visible light response semiconductor photocatalytic materials for environmental remediation.

Bismuth oxybromide, BiOBr, as a highly anisotropic and unique layer-structured indirect semiconductor [17-20], has stimulated considerable interests for applications in photocatalytic degradation, hydrogen evolution, nitrogen fixation and carbon dioxide reduction [21, 22]. The unique layered structure of BiOBr can effectively polarize the corresponding atoms and *p*-orbitals, leading to high mobility of photogenerated charge carriers induced by dipole moments [23]. Moreover, owing to the indirect transition bandgap and intrinsic static electric field between $2Br^-$ and $[Bi_2O_2]^{2+}$ layers, the stimulated electrons can be easily excited via a certain *k*-layer, which is conducive to inhibiting the recombination of electron-hole pairs and thereby improving photocatalytic performance [24, 25]. Nevertheless, the activity and solar-conversion efficiency of BiOBr are still limited by several drawbacks, such as undesirable particle size, large bandgap and unsuitable energetic band structure [26-28]. To address these limitations, considerable research has been conducted to promote the catalytic performance, including construction of heterojunction, vacancy engineering and loading with noble metal particles [29-31]. However, these complicated processes and high cost make these techniques unsuitable to meet higher-volume, practical and affordable industrial needs [32, 33]. Hence, it is imperative to develop a facile and feasible strategy for synthesizing superior BiOBr photocatalysts to satisfy practical demand.

Polyvinyl pyrrolidone (PVP) as a capping agent has aroused significant attention in the synthesis of catalysts due to its non-toxicity, high stability, bio-compatibility and steric effect [34, 35]. Endowed with these desirable properties, PVP is a promising candidate material for the modification of nanocrystals including adsorption adjustment, chiral modification and charge carrier transfer promotion to improve the activity of catalysts [36, 37]. For instance, PVP assisted $ZnCo_2O_4$ nanoparticles with ring-like morphology exhibited a higher specific capacitance as compared to rods, hexagonal-like and oval “rice grain” morphologies [38]. The enhanced efficiency was ascribed mainly to the hierarchical structure with numerous spherical nanoparticles, which was synthesized with the addition of a suitable amount of PVP and forming an easier transfer pathway for electrons. Gracita et al. developed $ZnCo_2O_4$ and $NiCo_2O_4$ nanoparticles supported by PVP as a growth modifier and surface stabilizer [39], which demonstrated both remarkably high activity and high durability in oxygen evolution reactions. PVP plays an essential role in heterogeneous catalyst synthesis, which can efficiently inhibit catalyst aggregation as well as precisely control the structural properties. Based on these prior studies, modification of BiOBr catalysts with a PVP capping agent is expected to be a highly efficient and facile strategy to achieve superior catalytic activity. Although various studies have widely utilized PVP as a modifier to improve the catalytic performance of catalysts, the systemic mechanism and adverse impact of excessive PVP should be further explored and clarified.

In this work, a facile precipitation method was firstly utilized to fabricate BiOBr-PVP composites under ambient conditions. By varying the mass ratio of PVP, the surface morphology, particle size and photocatalytic performance of the BiOBr catalyst all exhibited a response. Furthermore, the strong interfacial coupling, tunable bandgap structure and greater exposure of reactive sites by introducing PVP could effectively accelerate the charge carrier separation and migration. Benefiting from the individual advantages of BiOBr and PVP, BiOBr-PVP composites not only display high photooxidation activity for organic dyes and tetracycline (TC), but also photoreduction for Cr(VI) ions under visible light. The excellent catalytic performance under solar irradiation and desirable stability render BiOBr-PVP catalysts as promising candidates for further development towards application in wastewater treatment.

2. Experimental Procedures

2.1. Chemicals

$Bi(NO_3)_3.5H_2O$, KBr, Polyvinylpyrrolidone (PVP), absolute ethanol, rhodamine B (RhB), $K_2Cr_2O_7$, p-benzoquinone, triethanolamine, and isopropyl alcohol were purchased from Sinopharm Chemical Reagent Co., Ltd., China. All reagents used were analytical-grade reagents.

2.2. Fabrication of BiOBr photocatalysts

The BiOBr-PVP samples were prepared via a facile one-step co-precipitation method. Firstly, 1.02 g of $Bi\ (NO_3)_3\cdot 5H_2O$ was stirred magnetically at room temperature in 60 mL of ethanol for 60 min to obtain a homogenous white suspension. Then, a certain amount of PVP (0.02 g, 0.05 g, 0.1 g, 0.2 g and 0.4 g) was added into this mixture, which was then stirred for a further 60 min. Following this, 0.0833 g KBr was added to obtain a white precipitate. After stirring for a further 12 h, the resulting precipitate was centrifuged and washed with deionized water and absolute ethanol six times. Finally, the product was transferred to a vacuum drying oven and dried at 60°C overnight. As a comparison, pure BiOBr was synthesized using the same procedure but without addition of PVP. The products synthesized with 0 g, 0.02 g, 0.05 g, 0.1 g, 0.2 g, 0.4 g PVP were labeled as BiOBr, B-0.02, B-0.05, B-0.1, B-0.2, B-0.4, respectively.

2.3. Characterization

X-ray diffraction (XRD) patterns detected by X-ray diffractometry were applied to evaluate the crystal structure of the samples. Fourier transform-infrared (FT-IR) spectra were obtained using an FT-IR optical spectrometer (Nexus 670) in the range 500-3500 cm^{-1}. The morphology and composition of BiOBr were analyzed by scanning electron microscopy (SEM, FEI Quanta FEG250), transmission electron microscopy (TEM, JEM-2100F) and energy-dispersive X-ray spectroscopy (EDX). Surface electronic states were recorded by X-ray photoelectron spectroscopy (XPS, VG MultiLab 2000). The N_2 adsorption-desorption measurements were analyzed by the nitrogen adsorption apparatus (ASAP 2020, USA). The UV-vis diffusive reflectance spectra (DRS) of samples were analyzed on a UV-vis spectrophotometer (U3010). Photoluminescence (PL) spectra were obtained by fluorescence spectrometry (FP-6300). Total organic carbon (TOC) was measured by a TOC analyzer (Aurora 1030S).

2.4. Photoelectrochemical analysis

Electrochemical impedance spectroscopy (EIS) and Mott-Schottky measurement were carried out using a three-electrode system of a CHI-600E electrochemical workstation (Shanghai Chenhua, China). A Pt plate and saturated calomel electrode were used as the counter electrode and reference electrode. The measured samples were fixed onto an FTO glass (1×1 cm) and these were used as the working electrode, and 0.1 M Na_2SO_4 aqueous solution was used as the electrolyte.

2.5. Photocatalytic activity and stability

To assess the photocatalytic performance of the as-prepared photocatalysts, RhB, tetracycline (TC) and Cr(VI) aqueous solutions were used as target pollutants. A 100 W Xenon lamp (XPA, Xujiang Electromechanical Plant, Nanjing, China) equipped with a series of cut-off filters ($\lambda \geq 420$ nm) was used as the light source. Here, 20 mg of fine photocatalyst powder was completely dissolved into 100 mL (20 mg • L^{-1}) of RhB aqueous solution and 100 mL (10 mg·L^{-1}) of Cr(VI) aqueous solution, respectively. The suspension was subjected to vigorous stirring for 1 h to attain adsorption-desorption equilibrium and then maintained to be irradiated by the Xe lamp. During the process of reaction, 3 mL RhB suspension was sampled at every 10 min interval and 3 mL of Cr(VI) suspension was sampled at every 20 min interval. The whole process lasted for 2 h. The collected samples were all filtered using a 0.45 μm membrane and were measured for RhB concentration at a wavelength of 554 nm using a UV–Vis spectrophotometer. Cr(VI) concentration was determined by the Diphenyl carbazide spectrophotometric method. The photooxidation intermediates of TC were measured using the LC-MS system (6460 Triple Quad). To further detect the photoactivity of the sample catalysts, photodegradation measurements were conducted under solar light irradiation, which was tested between 12:00 pm to 14:30 on sunny days, in the city of Qingdao, China (GPS coordinates: N=36.04°, E=120.19°). The range of temperature during the measurements was 30-34°C and the intensity of solar irradiation varied in the range 14.0-14.8 mW/cm^2. The repeatability and stability of photocatalysts were confirmed by repeating the experiments above 4 times each.

2.6. Photocatalytic mechanism

To investigate the photocatalytic mechanism of BiOBr catalyst, isopropyl alcohol (IPA), benzoquinone (BQ) and triethanolamine (TEOA) were used as sacrificial agents for hydroxyl radicals (•OH), superoxide radicals ($\bullet O_2^-$) and holes (h^+), respectively, via in-situ trapping experiments. The experimental process for the primary reactive species is similar to that used for the RhB photodegradation, except here the IPA, BQ and TEOA were used at 20, 0.1, 0.2 mmol·L^{-1} concentration, respectively.

2.7 Computational details

The electronic structures and properties of BiOBr and BiOBr-PVP samples were simulated by the first-principles method based on density functional theory (DFT) implementing CASTEP software. Generalized Gradient Approximation (GGA) and Perdew-Burke-Ernzerhof (PBE) functional were used for structural optimization and general property calculations. Periodic boundary condition was applied in X, Y, and Z direction, and a large vacuum layer of 25 Å was applied in Z direction to eliminate the influences from adjacent layers. BFGS method was used for the geometry optimization and the energy cut-off for the plane wave expansion was chosen to be 400 eV, leading to a convergence of residual force tolerance and total energy to be 0.03 eV/atom and

1.0×10^{-6} eV/angstrom, respectively. Grid of 9×9×1 was used for single-point energy and property calculations.

3. Results and discussion

3.1. Characterization of catalysts

The morphology and microstructure of the BiOBr catalysts were characterized by SEM and TEM analysis. As depicted in Fig.1a-d, pristine BiOBr and BiOBr-PVP composites showed similar morphologies, namely, self-assembled flower-like hierarchical structures of uniformly numerous BiOBr lamellae. The average size of these BiOBr-PVP hybrids lamellae was ~2 μm, which was smaller than for pure BiOBr (~3-3.5 μm). The diminished particle size parameters were further identified using the Brunauer-Emmett-Teller method (Table S1). The 2D nanosheets with smaller size could efficiently expose more active sites per unit area on the surface and thus improve catalytic activity and accelerate charge carrier transfer via reduced carrier diffusion lengths [40, 41].

As shown in Fig.S1, the high-resolution TEM observations also confirmed the ultrathin and "wrinkled" sheet structure of the BiOBr catalyst, which interact with each other to form a porous network with micrometer-sized pores (Table S1). The continuous interplanar lattice fringes of 0.277 nm in both the BiOBr and BiOBr-PVP composites (Fig. 1e-f) were matched with the highly reactive single crystal (001) facet, which could not only promote the separation of electron-hole pairs by the potential driving force but also increase the diffusion of photogenerated electrons toward more uniformly on the catalyst surface [31]. In comparison with pristine BiOBr, the lattice fringes observed for the BiOBr-PVP composite are less well-defined due to shielding effects caused by introduction of the PVP capping agent. According to SEM-electron microscopy-energy dispersive X-ray spectrometry (EDX) elemental mapping of sample B-0.05, it can be clearly observed that Bi, O and Br were homogeneously distributed and the elemental atomic ratio of Bi/Br is approximately 1 (Fig. S2), consistent with the successful in-situ formation of BiOBr. Moreover, it was demonstrated that the atomic percentage of O was approximately 2 double that of Bi and Br, which is attributed to O in the PVP and the aggregation of PVP in the red area (Fig. 1g) [42].

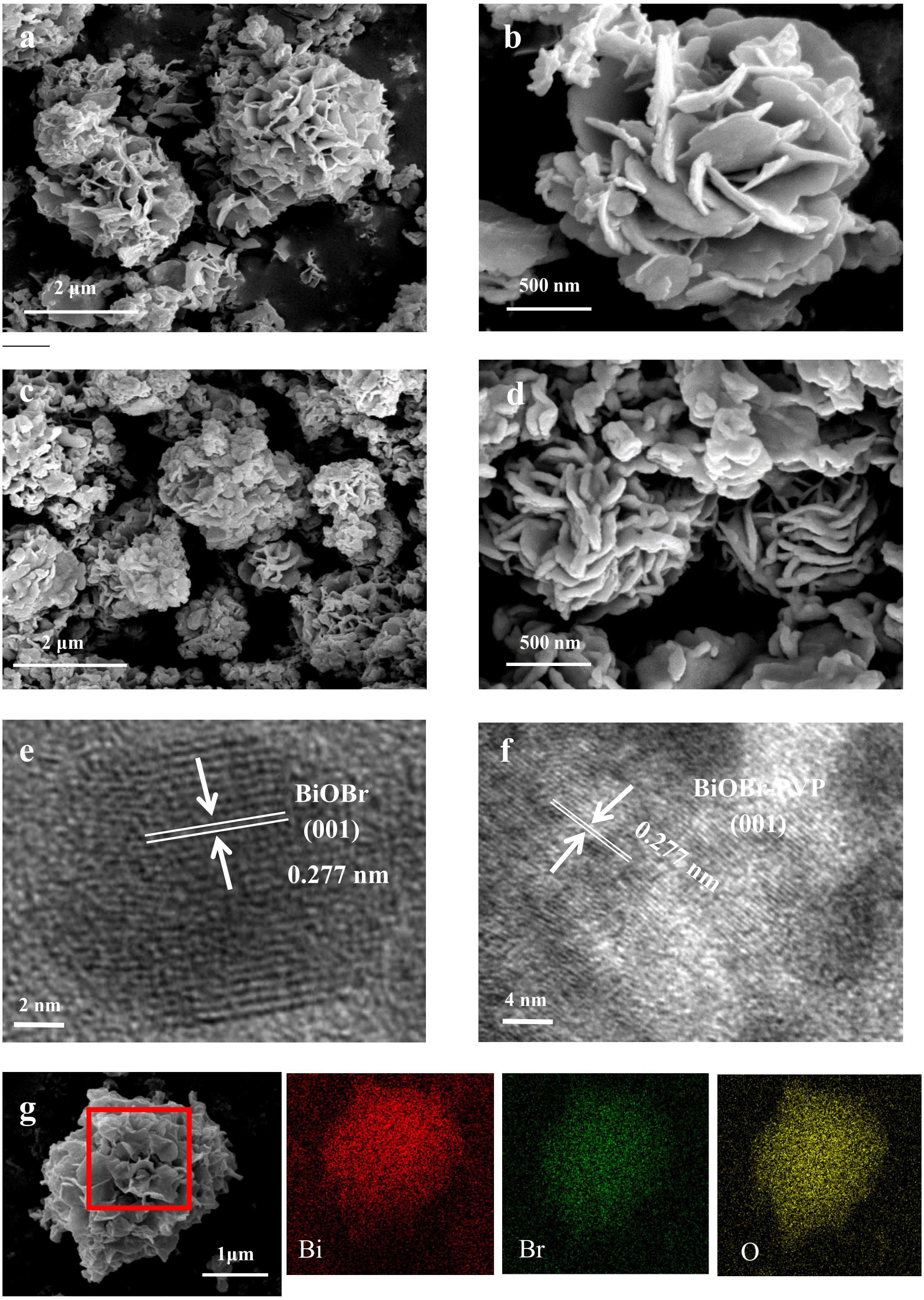

Fig. 1. SEM images of (a, b) pristine BiOBr, (c, d) B-0.05. TEM images of (e) pristine BiOBr, (f) B-0.05. (g) EDX elemental mapping of the rectangle region indicated by the red border.

The crystalline phases present in the BiOBr catalysts were characterized by X-ray diffraction (XRD). As displayed in Fig.2a, diffraction peaks of BiOBr were observed at 2θ of 10.8°, 21.9°, 25.2°, 31.7°, 32.3°, 39.5°, 42.6°, 46.2°, 53.4°, 57.1° and 67.4°. These correspond to (001), (002), (101), (102), (110), (112), (004), (200), (211), (212) and (220) crystal planes, respectively, which are consistent with the successful fabrication of single-phase tetragonal BiOBr (JCPDS card No. 73-2061) catalyst [43]. After addition of PVP, the half-width became broader and less intensity in the BiOBr-PVP hybrids compared with pristine BiOBr. This is attributed to the decreased particle size which can effectively inhibit the agglomeration of catalysts and improve the dispersibility [44]. No impurity phases were detected in the diffraction patterns of the BiOBr/PVP composites, indicating the single-phase, highly crystalline nature of the as-prepared catalysts. The X-ray diffraction results were well matched with the *d*-spacing of (001) facet (0.277 nm) observed by TEM measurement.

The surface chemical structures of the BiOBr and BiOBr-PVP catalysts were investigated by Fourier transform infrared absorption spectroscopy (FT-IR). As shown in Fig. 2b, the characteristic peak at around 520 cm^{-1} was identified as the Bi-O stretching mode [45]. For BiOBr-PVP composites, a new absorption peak at 1280 cm^{-1} was attributed to the tensile vibration of C-N heterocyclic ring in PVP, indicating the successful integration of the two phases [46]. The strong absorption peaks at ~1400-1500 cm^{-1} were attributed to vibrations of –CH$_2$, –OH and –COO– bonds [47], while the band located at 1690 cm^{-1} may be due to the typical C=O stretching vibration in carboxyl group [48]. The broad peaks at 3150 cm^{-1} and 3400 cm^{-1} were attributed to the stretching motion of N-H and O-H bonds in PVP and absorbed water molecules [42]. The characteristic band at 1660 cm^{-1} in the spectra for BiOBr-PVP composites demonstrated an obvious blue shift compared to PVP, which is ascribed to the strong interfacial coupling and the electron transfer between BiOBr and PVP.

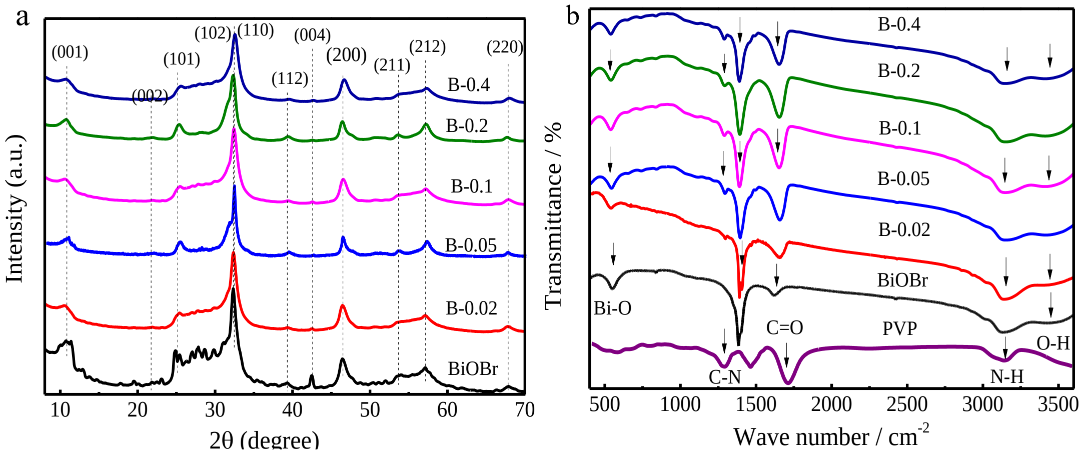

Fig. 2. (a) XRD patterns and (b) FT-IR spectra of BiOBr, B-0.02, B-0.05, B-0.1, B-0.2 and B-0.4.

The surface chemical states of the BiOBr catalysts were studied by X-ray photoelectron spectroscopy (XPS). As observed in Fig. S3, the full spectrum indicated that Bi, Br and O coexisted on the surface of BiOBr and B-0.05 catalysts. In the high-resolution spectrum for Bi 4f (Fig.3a), two peaks at 158.9 eV and 164.2 eV were fitted for the Bi 4f$_{7/2}$ and Bi 4f$_{5/2}$ electrons, respectively. However, these two characteristic peaks were observed to have slightly higher binding energies by ~ 0.3 eV for the B-0.05 composite, suggesting strong chemical interaction between BiOBr and PVP. The Br 3d spectrum was fitted into two peaks, including 68.34 eV for Br 3d$_{5/2}$, and 69.41 eV for Br 3d$_{7/2}$, respectively. The atomic ratio of Bi to Br was found to be 12.9:13.6, which is consistent with the EDX mapping analysis, illustrating the high purity of as-prepared BiOBr catalyst. The binding energy of the Br 3d peak shifted to lower energy by 0.2-0.3 eV compared with pristine BiOBr, indicating changes in chemical coordination / local environment [30]. For the O 1s spectra, the peak can be fitted with various O species at 529.7 eV, 530.8 eV and 532.0 eV, which arise from the oxygen species in $Bi_2O_2^{2+}$, Bi-O chemical groups and O-H bonds [47], respectively. The shifted binding energies in the Bi, Br and O spectra imply electronic coupling between BiOBr and PVP components [49]. Furthermore, the high-resolution C 1s spectra (Fig. S3) manifest as three major peaks at 284.6 eV, 285.7 eV and 287.5 eV. These correspond to the sp^2 C=C/ C-C, C=O/C-O and C-N groups[46], respectively. The spectra for N 1s (Fig. S3) showed a single peak at 399.58 eV, corresponding to the N-H bond [46]. Both C1s and

N1s spectra were observed in the B-0.05 XPS spectra, which are attributed to carboxyl, methyl and amino groups of PVP [50].

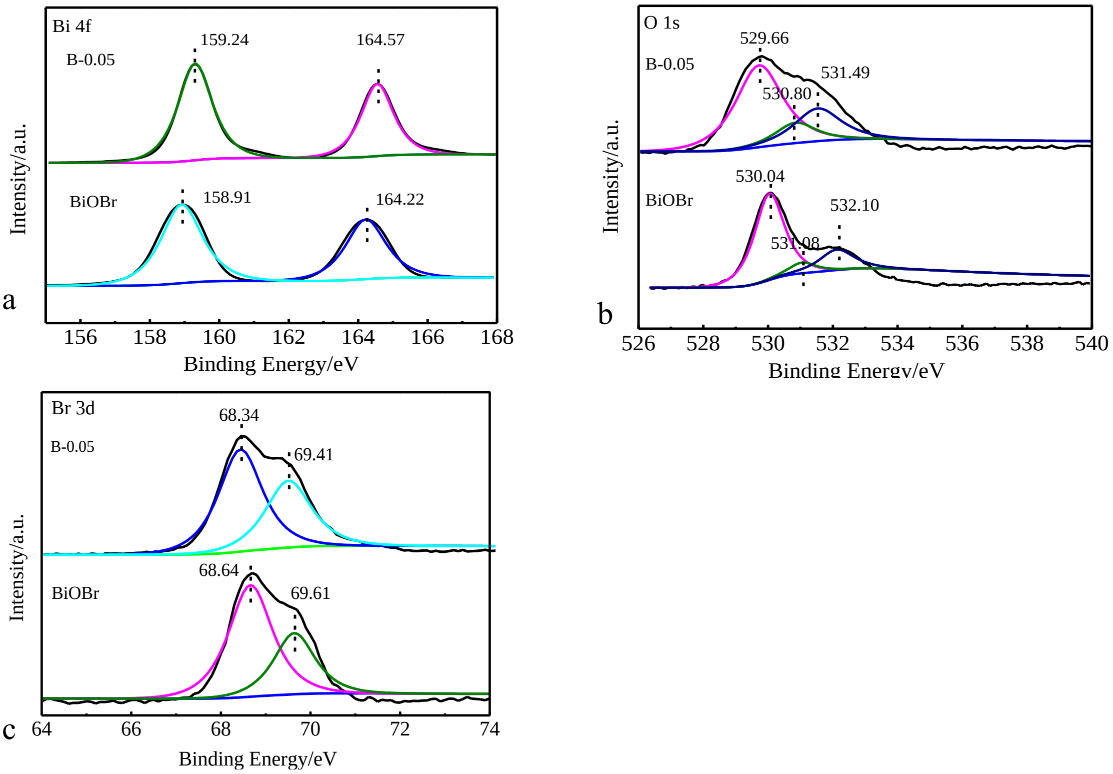

Fig. 3. XPS spectra of BiOBr and B-0.05: (a) Bi 4f, (b) Br 3d, (c) O 1s.

As shown in Fig. 4a, all BiOBr-PVP catalysts showed Type III N_2 adsorption–desorption isotherm characteristic with a hysteresis loop [51]. The specific surface areas of the catalysts were calculated to be 12.48, 17.18, 20.53, 22.35, 17.44 and 13.84 m^2/g, respectively by Brunauer-Emmett-Teller (BET) method. Increasing the PVP content from 0 to 0.4 g results in a volcano curve of specific surface area and pore volume. Owing to the larger surface area and pore volume by comparison with the pure BiOBr catalyst, the B-0.05 catalyst provided greater contact area and channels for interactions between active sites and pollutants [52], which could significantly promote catalytic activity with less resistance [53]. The corresponding pore diameters of BiOBr, B-0.02, B-0.05, B-0.1, B-0.2 and B-0.4 catalysts were estimated to be 31.7, 28.8, 21.2, 27.8, 29.0 and 30.6 nm (Table. S1), respectively via the Barrett–Joyner– Halenda (BJH) method, indicating the catalysts are mainly ascribed to mesopores (2-50 nm). During the synthesis process, the Bi^{3+} ions in the precursor could react with PVP to form [(Bi^{3+})

$_x$(PVP)$_y$] intermediates. Owing to the addition of excessive PVP, the Bi^{3+} centers were always coordinated with this capping agent and the growth rate correspondingly decreased, resulting in aggregation of the molecules and eventually enlarging particle size (Fig. 4c). Generally, smaller nanoparticle sizes can produce more defects on the catalyst surface and significantly promote catalytic performance [54].

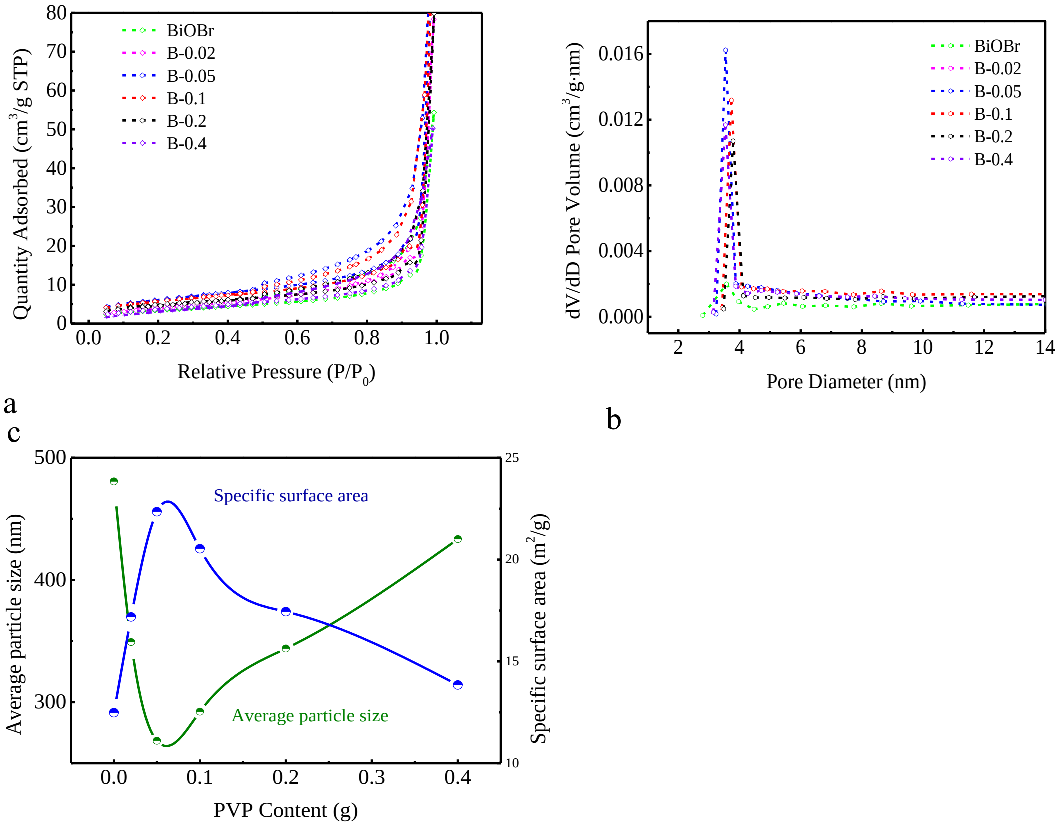

Fig. 4 (a) N_2 adsorption/desorption isotherms, (b) Pore size distribution of all catalysts, (c) PVP content dependence of the Specific surface area and average particle size

3.2. Photocatalytic activity of BiOBr-PVP catalysts

3.2.1 Photocatalytic oxidation activity of organic dyes

The photocatalytic oxidative properties of as-prepared catalysts were investigated by decomposing Rhodamine B (RhB) under visible light irradiation. To explore the absorption ability of BiOBr, a series of adsorption experiments were firstly conducted under a dark environment. As shown in Fig. S4, all catalysts could reach adsorption equilibrium within 60 min and the B-0.05 catalyst exhibited the highest adsorption capacity due to having the largest surface area and pore volume, which could efficiently accelerate transport between reactant molecules and the catalysts.

After achieving adsorption-desorption equilibrium, the photocatalytic oxidation experiments were carried out under visible light illumination. As exhibited in Fig. 5a, only 53.14% of RhB was degraded within 40 min by pristine BiOBr, mainly due to less catalytic active sites and higher photogenerated carrier recombination efficiency [55]. As expected, the BiOBr-PVP composites exhibited superior photocatalytic performance, illustrating the synergistic effect between BiOBr and PVP in pollutant oxidation processes. Moreover, the photocatalytic activity of BiOBr-PVP composites is dependent on the amount of PVP. The RhB removal efficiency gradually increased and then decreased with PVP loading amount from 0.02 g to 0.4 g. Sample B-0.05 manifested the highest RhB removal efficiency of 99% after 40 min, whilst 94.75, 91.24 and 77.83% of RhB was decomposed using the B-0.1, B-0.2 and B-0.4 catalysts. This result revealed that the interfacial interaction between BiOBr and PVP is an essential factor. A suitable content of PVP could expose more photocatalytic reaction sites, and provide more binding sites for transfer and separation of charge carriers [56]. To further evaluate catalytic activity of sample B-0.05, the mineralization conversion efficiency of RhB was measured (Fig. S5). It can be noted that the mineralization of RhB is about 60% within 60 min under visible light irradiation, demonstrating the rapid mineralization capacity of B-0.05. Interestingly, the mineralization conversion efficiency was lower than the degradation rate. This is attributed to the effects of the organic intermediates generated during photodecomposition [57].

The photodegradation of RhB was shown to follow the Langmuir Hinshelwood dynamic model [58] for cases in which the concentration of simulated wastewater is relatively low. The corresponding reaction equations are described as follows:

$$r = k\theta_A = kK_A C_A/(1 + K_A\, C_A) \tag{1}$$

The kinetic expression (1) was modified to：

$$\frac{1}{r} = \frac{1}{kK_1} \cdot \frac{1}{C_A} + \frac{1}{k} \tag{2}$$

When the value of C is extremely small, $K_A C_A \leq 1$, (2) can be simplified to：

$$r = kK_AC \quad (3)$$

After integral of expression (3)：

$$\ln(C_0/C) = k_1t \quad (4)$$

Where C_0 and C are the concentrations of the dye at t=0 and t, $k_1=k$, K_A is the apparent first-order reaction rate constant.

As plotted in Fig. 5c, there is a clear linear relationship between $\ln(C_0/C)$ and t, indicating the photocatalytic degradation process fit well with pseudo-first-order reaction kinetics. The apparent rate constants of BiOBr, B-0.02, B-0.05, B-0.1, B-0.2 and B-0.4 were 0.021, 0.058, 0.12, 0.072, 0.058 and 0.048 min^{-1}, respectively, which vary with the doping amount of PVP as a volcano curve. The k value of B-0.05 is 5.7 times higher than that of pristine BiOBr. This is ascribed to the higher adsorption ability and greater abundance of binding sites of the hybrid composite materials. Considering the determining effects of specific surface area and particle size on the efficacy of the photocatalytic process, the BET surface area normalized rate constant (k_{BET}) was calculated and k_{BET} values of composites were calculated to be 0.0034, 0.0058, 0.0032, 0.0033, 0.0034 min^{-1} m^{-2}, respectively, which were about 2.01, 3.47, 1.91, 1.97, 2.06 times that of pure BiOBr (0.0016 min^{-1} m^{-2}), indicating that the structural properties of the catalyst play a critical role in catalytic activity.

Fig. 5b displayed the temporal evolution of UV-vis absorption spectra of RhB by the B-0.05 catalyst. It can be seen that the intensity of the absorption peak centered at 554 nm gradually decreased and tended to disappear after 40 min. Meanwhile, the color of the RhB solution changed from transparent pink to colorless, suggesting that the B-0.05 composite could achieve complete decolorization for RhB. After 10 mins, the maximum absorption wavelength shifted from 554 nm to 500 nm, consistent with the formation of rhodamine (500 nm) during the N-demethylation process [59]. In addition, the photocatalytic activity of RhB over several catalysts under solar light irradiation was presented in Fig. 5d. After 100 min illumination, the degradation efficiency of BiOBr, B-0.02, B-0.05, B-0.1, B-0.2, B-0.4 were 73.1, 90.6, 98.9, 95.8, 90.8 and 88.0%, respectively, and the highest efficiency was also obtained by the B-0.05 catalyst, which agreed with the activity by Xenon lamp irradiation. Moreover, the corresponding rate constants (*k*) of BiOBr-PVP composites were calculated to be 0.023, 0.045, 0.032, 0.023 and 0.021 min^{-1}, respectively, which were far higher than pristine BiOBr (0.013 min^{-1}), further demonstrating the enhancement in performance and thus excellent potential for practical application.

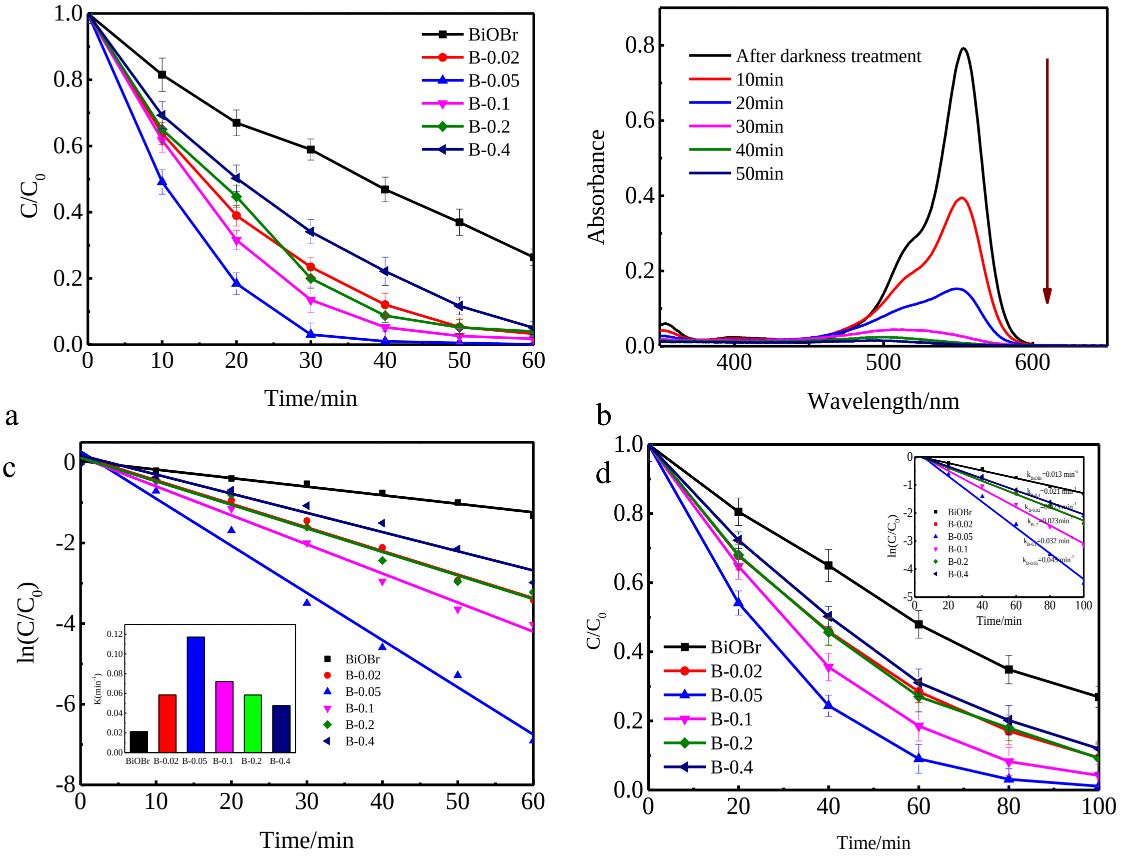

Fig. 5. (a) Photodegradation of RhB with all catalysts under visible light, (b) Absorbance of RhB solutions photocatalyzed by B-0.05, (c) The first-order-kinetic plots and corresponding apparent rate constants *k* of all catalysts, (d) Photodegradation of RhB with all catalysts under sunlight irradiation.

The effect of catalyst (B-0.05) dosage on the photocatalytic performance was illustrated in Fig. 6a. As is expected, the removal efficiency of RhB gradually increased with the catalyst dosage increase, due to an increased number of exposed active sites and better visible light response at higher catalyst dosage. The degradation rate of 97% can still be obtained within 30 min for the catalyst dosage of 0.3 g·L^{-1}, which only exhibited a slight drop compared with the dosage of 0.5 g·L^{-1} (98.7%). Considering the cost consumption and catalytic performance, the catalyst concentration of 0.3 g·L^{-1} is thought to be an optimal value in the purification of wastewater.

To further explore the catalytic activity of sample B-0.05, various organic dyes such as MO and MB were selected and degraded under the same conditions. As shown in Fig. 6b, these organic dyes could be efficiently decolorized and degraded within 80 min under visible light irradiation. In comparison with MO, RhB and MB without azo bonds (-N=N-) in the molecular structure (Fig. S6) are positively charged in aqueous solutions [60, 61]. In the process of MB photodegradation, the diethylamino group $(C_2H_5)_2$-N-, can be effectively transformed into $-NH_2$ by removing the ethyl group, and then oxidized to form NH_4^+ by photo-generated holes and hydroxyl radicals. Meanwhile, the benzene ring can be attacked and oxidized to small molecular substances via carbon-carbon bond cleavage, which eventually achieves thorough decomposition. Owing to the existence of p-substituted $-SO_3H$ groups, the anionic dye MO exhibited electrophile and conjugation effect. During the photocatalytic process, the azo bond (-N=N-) can be firstly broken by photoinduced hole-electron pairs and then further totally degraded. As displayed in Fig.6b, the removal efficiency of RhB, MB and MO pollutants could be achieved to 99.0, 85.6% and 71.1% within 40 min, and the corresponding first-order kinetic constants were 0.098, 0.014 and 0.048 min^{-1}, respectively, which might result from the different adsorption ability of anionic and cationic dyes. To explore this point, the adsorption capacity for three dyes by B-0.05 was measured (Fig.6c). The rate of RhB adsorption by B-0.05 was 44.5%, which was 1.68 and 4.02 times higher than MB and MO, further supporting the view that average surface charge of the molecules determined the phase transfer efficiency of dyes during the photocatalytic process. Furthermore, the addition of PVP resulted in decreased diameters of B-0.05 nanosheets, thereby increasing the exposed reactive (001) crystal facets, which improved the percentage of highly reactive sites and negative electrical charge density along the (001) plane, thus enhancing the adsorption ability towards cationic dyes.

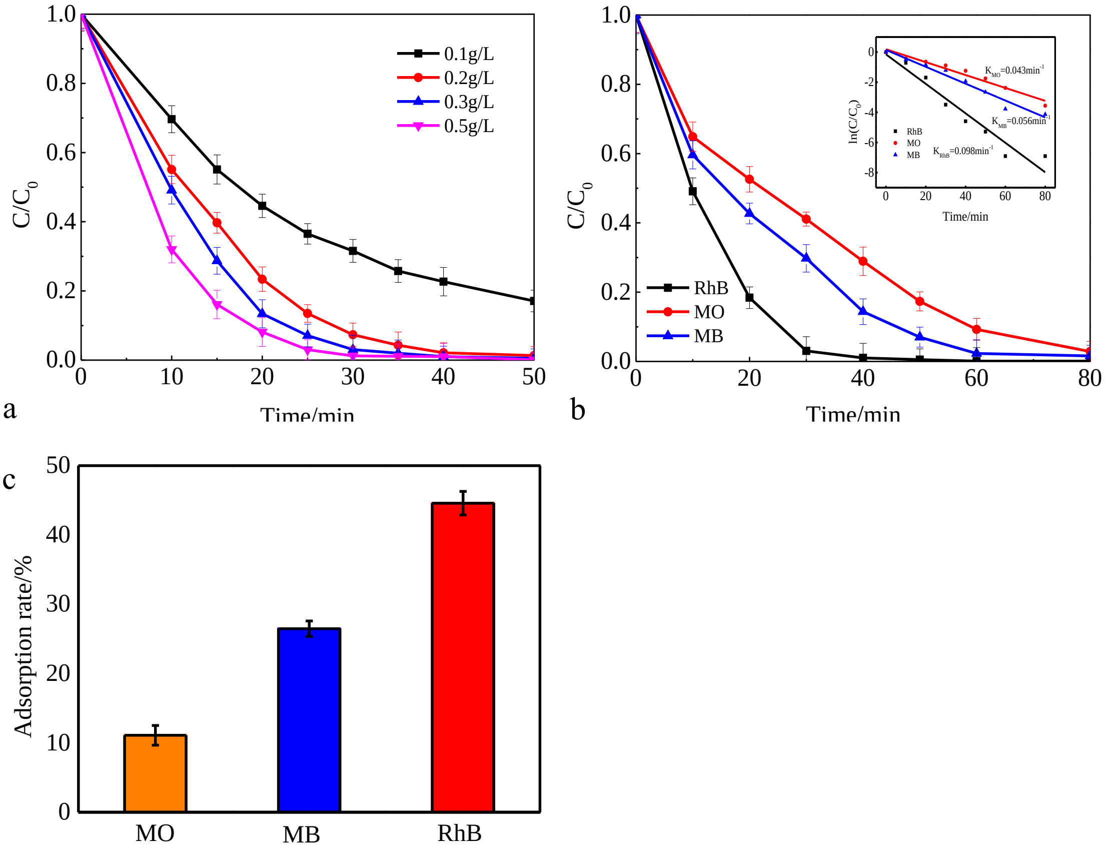

Fig. 6. (a) The effect of B-0.05 dosage on photodegradation of RhB, (b) The effect of B-0.05 on photodegradation of different dyes, (c) Adsorption rate of B-0.05 for different dyes.

3.2.2 Photocatalytic oxidation activity of TC

To avoid the influence of photocatalyst sensitized by dyes, refractory pollutant tetracycline was supplementary in this work. As plotted in Fig.7a, the TC can be effectively degraded by up to ～70% within 80 min, and the apparent rate constant *k* was also calculated to be 0.014 min^{-1} based on the pseudo-first–order dynamic equation of $\ln (C/C_0) = -kt$ (4). To clarify the oxidation process of TC, LC-MS measurement was carried out and the proposed oxidation pathway was illustrated in Fig. 7b. After the TC molecule (m/z=445) adsorbed onto the B-0.05 catalyst surface, the amine and phenol groups were firstly attacked by active species $\bullet O_2^-$, •OH and h$^+$. The intermediate compound with m/z=461 generated by hydroxylation of tetracycline derived from the high electron density of the double bond. The formation of intermediates with m/z=431 and m/z=417 mainly attributed to the N-demethylation reaction by h$^+$ attack. Furthermore, some substances with smaller molecular weights can be detected in the mass spectrogram, which were mainly decomposed under the combined effect of various radicals. Consequently, the corresponding degradation mechanism was proposed (Fig.7b), which was that $\bullet O_2^-$, •OH and h^+ attack the benzene ring and oxidize the $C(O)NH_2$ group and methyl group, leading to the benzene ring-opening and generation of new small intermediates (carboxylic acids). All of these intermediates were non-toxic and can be totally decomposed into inorganic molecules (such as CO_2 and H_2O). Overall, this result further proved that the B-0.05 catalyst possesses excellent oxidative effects for decomposing refractory organic pollutants such as TC.

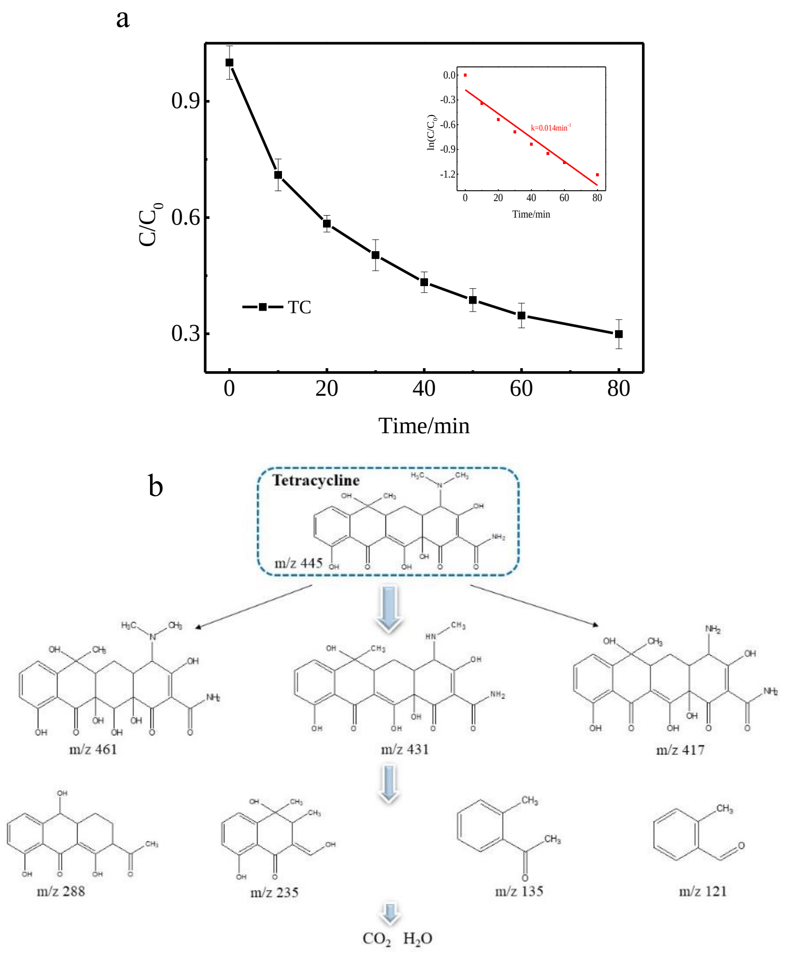

Fig. 7. (a) The photodegradation of TC by B-0.05, (b) The photooxidation intermediates of TC and the possible degradation pathway

3.2.3 Photocatalytic reduction activity of Cr(VI)

To investigate the photocatalytic reduction performance of BiOBr-PVP catalysts, the reduction efficiencies of hexavalent chromium to trivalent chromium by BiOBr, B-

0.02, B-0.05, B-0.1, B-0.2 and B-0.4 samples were measured, and are shown in Fig. 8a. It can be seen that the Cr(VI) reduction rate gradually increased as PVP content increased from 0 to 0.05 g, but further increases of PVP content led to a decrease Cr(VI) in reduction rate, which was consistent with the photocatalytic oxidation activity of each catalyst sample. After 160 min irradiation, the reduction efficiency of toxic Cr(VI) to Cr(III) were 64.9, 90.9, 79.3, 67.7 and 55.2% by B-0.02, B-0.05, B-0.1, B-0.2 and B-0.4, respectively, which were 2.38, 3.33, 2.91, 2.46 and 2.02 times higher than pure BiOBr. Furthermore, ln（C_0/C）is linearly related to the reaction time t (Fig. 8b), indicating the kinetics of Cr(VI) photoreduction also followed a pseudo-first-order reaction. As depicted in Fig. 8b, sample B-0.05 exhibited the highest reduction rate constant (k=0.0153 min^{-1}) compared with the other catalysts (k_{BiOBr}= 0.0019, $k_{\text{B-0.02}}$=0.0065, $k_{\text{B-0.1}}$=0.0097, $k_{\text{B-0.2}}$=0.0068 and $k_{\text{B-0.4}}$=0.0049 min^{-1}), which might be due to more efficient charge carrier separation and mobility [62]. The results elucidated that BiOBr-PVP catalysts have significance for the photocatalytic reduction of wastewater contaminated by Cr (VI).

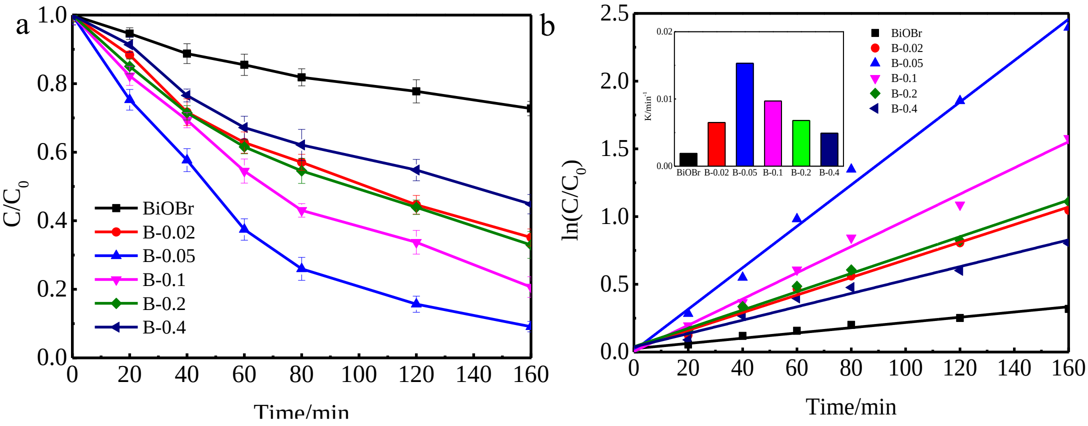

Fig. 8. (a) Photoreduction of RhB with all catalysts, (b) The first-order-kinetic plots and corresponding apparent rate constants k of all catalysts

3.2.4 DFT calculation: possible interaction between PVP and BiOBr

Generally, PVP can efficiently inhibit catalyst aggregation and overgrowth as well as control the structure and morphology in the synthesis process [63]. PVP can be described as “organic armor” restricting the free access of reactants to the metal surface, which results in strong interaction and electron transfer between PVP and the catalyst

(Fig.9a). To further explore the interaction and charge transfer between BiOBr and PVP, the First-principles calculations based on density functional theory (DFT) was carried out. Firstly, DFT calculation was used to calculate the surface energy of BiOBr surface (100), (010) and (001) planes. As shown in Fig.S7 and Table S2, the surface energy of BiOBr (001) plane is far higher than (100) and (010) planes, which could significantly increase the ratio of surface-active atoms and improve the catalytic process. Due to the inapparent periodic structure of polymeric compound, in this work, monolayer vinylpyrrolidone was chosen as an organic macromolecule for the construction of BiOBr-PVP composites model with reactive (001) plane. Considering the lattice periodic model, BiOBr of 2×2×1 supercell can fully accommodate the large molecules of vinylpyrrolidone and keep them as close as possible to simulate the chain structure of polymer.

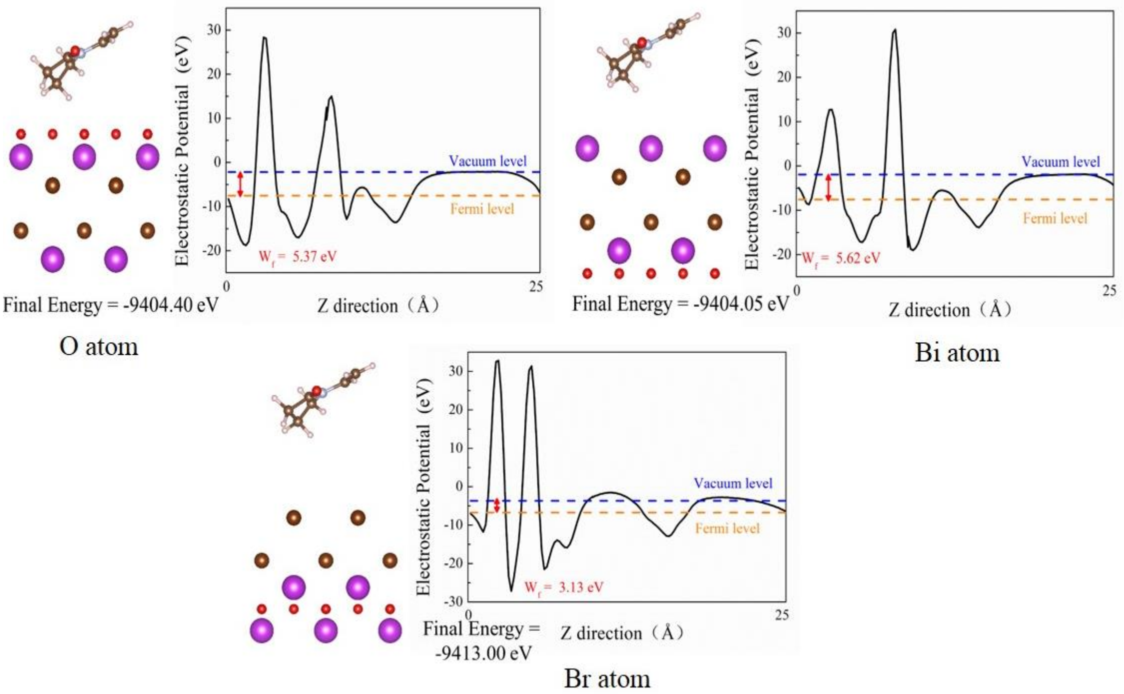

Fig. 9 Side view, electronic potential drop and final energy of the ball-stick crystal modes of BiOBr surface (001) plane (2×2×1) supercell combined with PVP (a) O atom as surface atom; (b) Bi atom as surface atom; (c) Br atom as surface atom

In BiOBr (001) plane, Bi, Br and O can become surface active atoms and interact with PVP, resulting in three different modes of interaction. Considering the maximization of photocatalytic activity and stability, the models between Bi, Br, O atoms and vinylpyrrolidone should be optimized based on the total energy and work function. During the photocatalytic process, work function along the interface indicates the charge carrier transport efficiency, which is an essential parameter to evaluate the photocatalytic performance of catalyst. As shown in Fig. 9, the final energy and electrostatic potential drop along the interface were calculated. It can be seen that the structure with Br as the surface atom exhibited lowest total energy and work function, indicating that it is the most stable and suitable structure for photocatalytic reaction. Due to the existence of van der Waals interaction between layers, the electrostatic potential drop along the interface was affected obviously. Moreover, the lower work function could reduce photocorrosion, accelerate the charge carrier separation efficiency, and thereby improve the catalytic efficiency.

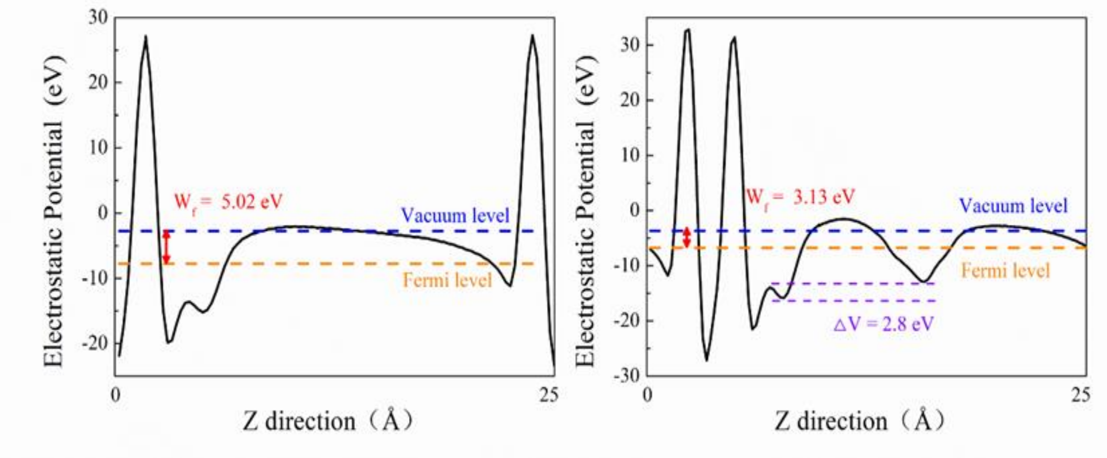

Fig. 10 The electrostatic potential and work function of pure BiOBr and BiOBr-PVP composite

Table 1. The average Mulliken charge density of Bi, O and Br atoms in pure BiOBr and BiOBr-PVP composite

Atom	Charge density of pure BiOBr	Charge density of BiOBr-PVP
Bi	1.33	1.21/1.32
O	-0.94	-0.92
Br	-0.39	-0.33/-0.37

To clarify the effect of PVP, the electrostatic potential, work function and average Mulliken charge density of Bi, O and Br atoms were calculated, as shown in Fig.10 and Table 1. In comparison with pure BiOBr, the work function along the interface significantly decreased, which attribute to the newly formed electric filed (~2.8 eV) in the interface of composite, leading to rapid separation and transport efficiency of photogenerated electron-hole pairs. Generally, the structure with uniform electric charge distribution is more conducive to the electrons transfer and decrease the bandgap energy of photocatalysts. Compared with pure BiOBr, the positive and negative charges in BiOBr-PVP composites obviously reduced, and the charge distribution tend to be more homogenization. This result indicated that the introduction of PVP not only changed the charge density and distribution of BiOBr, but also eventually decreased the bandgap energies. Because the average Milliken charge density of atoms in BiOBr close to the interface are more easily affected than that of far away from the interface, the Bi and Br atoms changed most obviously after combination of PVP.

Based on the DFT calculations and the experimental results, the versatile effects of PVP can be interpreted as follows: (1) PVP can effectively control the high energy surface of the catalyst (BiOBr), preventing aggregation and eventually reducing the particle size [64, 65]. (2) PVP can be selectively adsorbed on (001) planes of BiOBr, thereby leading to the anisotropic growth and high stability of nanoparticles [66]. (3) PVP could interact with the catalyst via non-covalent interactions as well as strong interfacial coupling, which could significantly accelerate charge-carrier transfer at the interface and promote catalytic performance. The addition of PVP improved the charge density and decreased the work function, which could accelerate charge transfer (Fig.11b) and reduce the bandgap energy.

On the other hand, it was pointed out that structural characteristics can be altered and damaged by introducing excessive amounts of PVP capping reagent. Owing to the extra complexity obtained from PVP, the content and cross-linking degree are crucial factors for catalyst synthesis (Fig.11c). It is widely recognized that an appropriate amount of surfactant induces the nanoparticles to be uniformly dispersed in solution. Superabundant PVP can act as a physical barrier and poison limiting the access of Br$^-$ to the Bi core and destroying the structure of the metal core. The solvation of PVP indicated dramatic adsorption and desorption from the BiOBr catalyst. Appropriate PVP molecules can easily attach to the catalyst and detach from the surface. On the contrary, low amount of PVP cannot be easily absorbed on the BiOBr surface while excessive contents tend to lead to agglomeration and suppression of catalyst growth (Fig.11c), which explains the catalytic performance trend as a function of PVP content being described by a volcano curve.

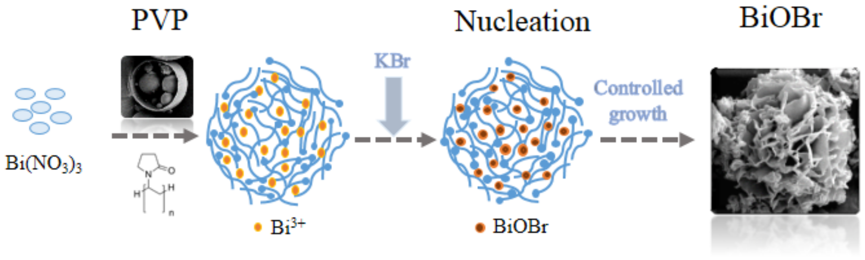

Fig. 11(a). Schematic process for the controlled formation of BiOBr-PVP composites

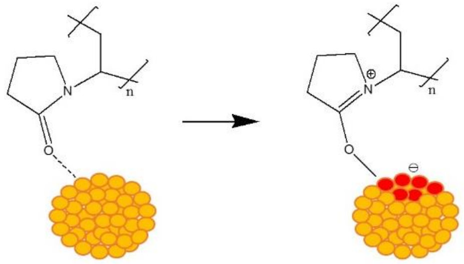

(b) Charge transfer between PVP and BiOBr

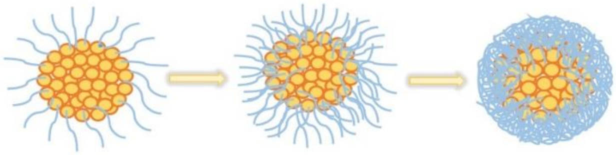

(c) Adsorption process on Bi core by PVP when PVP is of low, middle and high content

3.2.5. Stability analysis

The stability and recyclability of catalysts is crucial to practical wastewater treatment. Therefore, the catalytic reusability of B-0.05 composite was evaluated by performing a measurement over five cycles under visible light irradiation. After each recycle, the catalyst was separated by centrifugation, washed, vacuum dried and then used to the next cyclic experiment. As exhibited in Fig. 12a, the activity can maintain a stable level after each cycle, and the removal efficiency of RhB was still preserved above 90.0% after 60 min irradiation. The slight decrease in degradation rate may be due to trace loss and absorption of intermediates on the catalyst surface [67, 68]. Moreover, the morphology, crystal and chemical structure of B-0.05 were investigated by SEM, XRD and FTIR before and after reaction. The XRD pattern (Fig. 12b) and FTIR spectra (Fig. 12c) of used samples did not show a decrease in peak intensity and no new diffraction peaks appeared, indicating that the crystal and chemical structure were well-preserved after five cycles. The BiOBr-PVP catalyst still exhibited a flower-like spherical structure self-assembled by BiOBr nanosheets without any destruction (Fig. 12 c-d). The above analysis showed the excellent stability of the B-0.05 catalyst, underlining the great potential of BiOBr-PVP catalysts for large scale industrial applications.

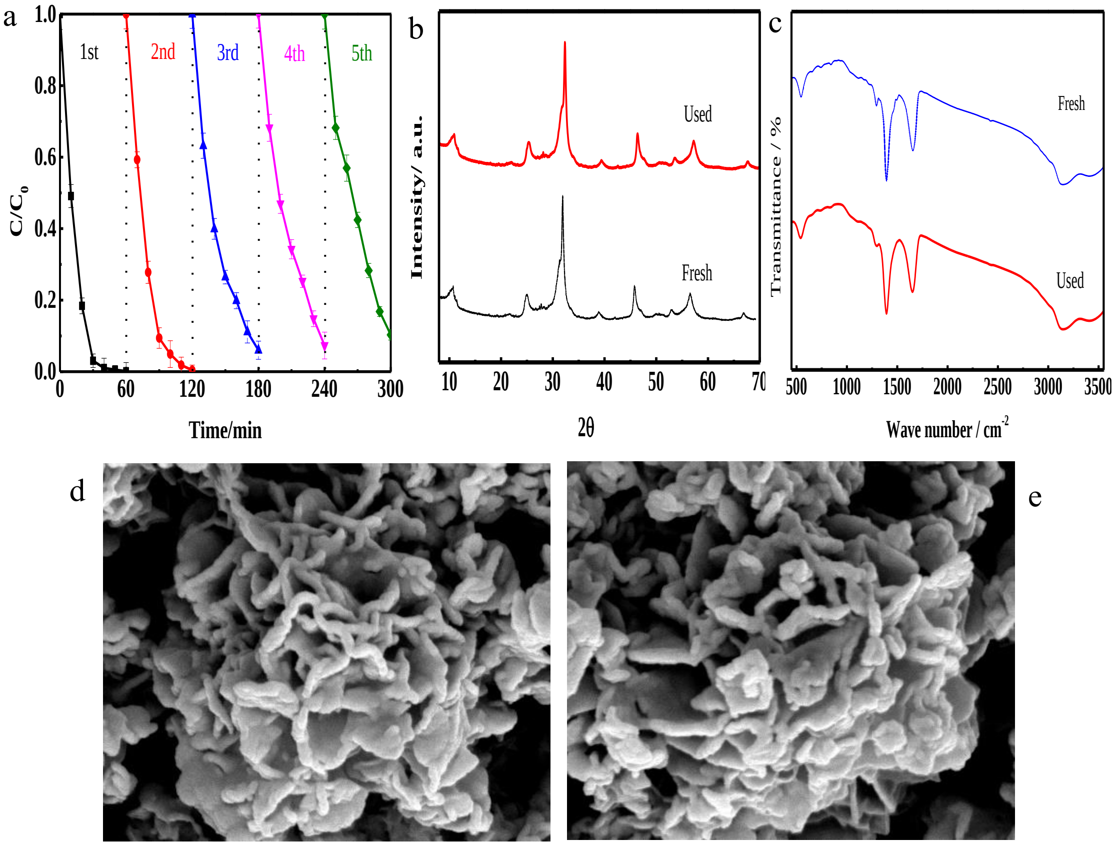

Fig. 12. (a)The stability test of B-0.05 driven by visible light, (b) XRD patterns, (c) FTIR spectra of B-0.05 before and after photocatalytic experiment, SEM of B-0.05 before (d) and after (e) photocatalytic experiment

3.3. Photocatalytic mechanism

Considering the excellent photocatalytic performance of BiOBr-PVP catalysts, the bandgap structure was evaluated to understand the optical properties. As shown in Fig. 13a, the UV–vis diffuse reflectance spectroscopy (UV–vis DRS) indicated that pure BiOBr possesses an absorption band edge of ～380 nm and BiOBr-PVP composites exhibited a positive shift in the visible region ranging from 400-430 nm. The improved harvest in luminous energy could be expected to induce more electron-hole pairs to participate in the catalytic process and thereby increase catalytic efficiency. The corresponding bandgap energy (E_g) can be calculated from a Tauc plots as follows： $\alpha(h\nu)= A(h\nu-E_g)^{n/2}$, Where α, h, ν, A are absorption coefficient, Planck’s constant, light frequency and a constant, respectively [69]. As an indirect transition, the n-value of BiOBr was selected to be 1 and the corresponding calculated bandgap energies (E_g) of

BiOBr, B-0.02, B-0.05, B-0.1, B-0.2, and B-0.4 were estimated to be 2.99, 2.96, 2.93, 2.90, 2.87 and 2.83 eV, respectively, which were gradually narrowed with increasing PVP amount in sequence, mainly ascribing to the intervalence charge transfer from PVP to BiOBr at the “core-shell” interface.

To further explore the band structure of the catalysts, the flat band edge positions were measured by the Mott-Schottky measurement. As displayed in Fig. 13c, the flat band potential of BiOBr, B-0.02, B-0.05, B-0.1, B-0.2 and B-0.4 were -0.54, -0.68, -0.56, -0.74, -0.60 and -0.68 V (vs Ag/AgCl), respectively, which were further calculated to be -0.40, -0.54, -0.42, -0.60, -0.46 and -0.54 V vs a normal hydrogen electrode (NHE) [70]. Generally, the flat band potential was about 0.1 V higher than the conduction band potential (E_{CB}) [71]. Therefore, the E_{CB} of BiOBr, B-0.02, B-0.05, B-0.1, B-0.2 and B-0.4 were corrected to -0.50, -0.64, -0.52, -0.70, -0.56 and -0.64 V versus NHE, respectively. The valence band potentials of these samples were calculated to be 2.49, 2.32, 2.41, 2.20, 2.31 and 2.19 V (Fig. 13d) by the equation (E_{VB}) = $E_g + E_{CB}$. Based on the above analysis, the band structures of BiOBr-PVP catalysts were summarized in Fig. 13d. The CB and VB positions of B-0.05 catalyst are located at -0.52 and 2.41 V, which could both generate highly active superoxide radicals ($\bullet O_2^-$, $O_2/\bullet O_2^-$=-0.33V) and hydroxyl radicals ($\bullet OH$, $OH^-/\bullet OH$=2.38V) during photocatalytic reaction.

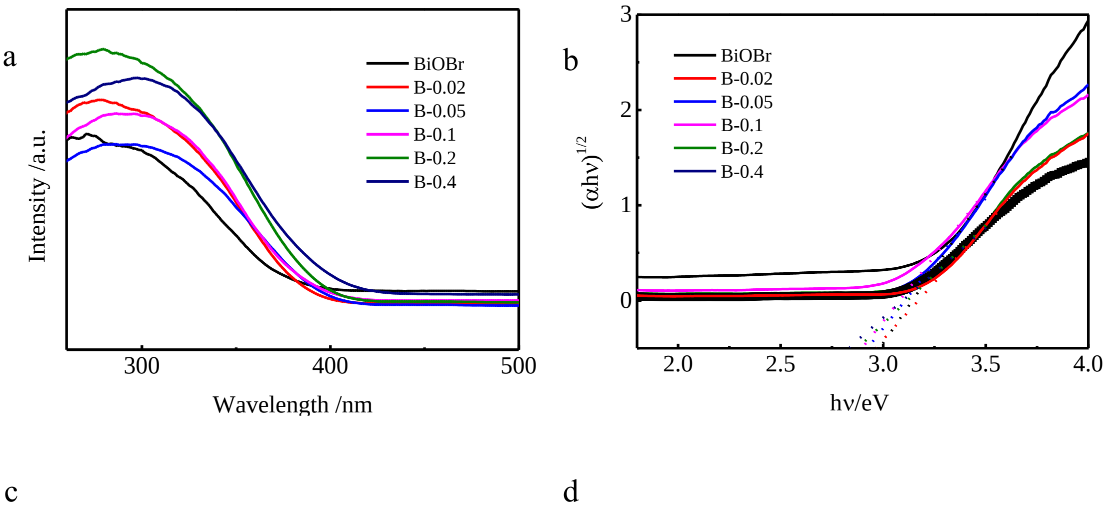

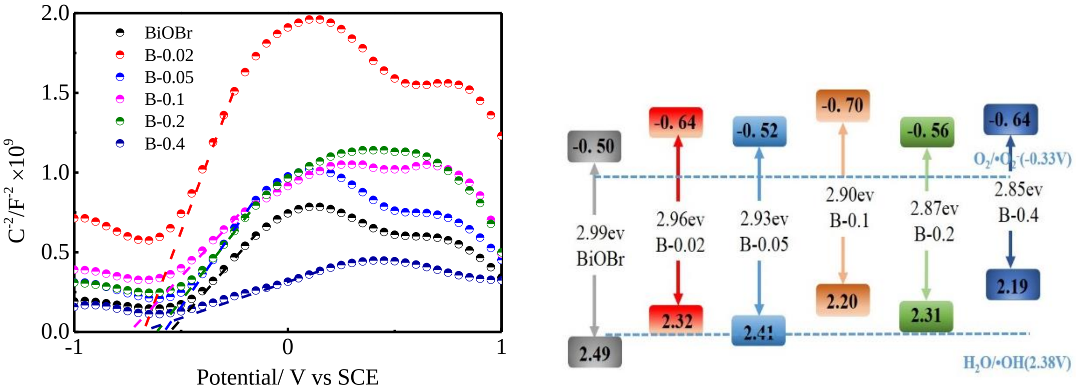

Fig. 13. (a) DRS absorption spectra, (b) The energy of bandgap, (c) Mott–Schottky plots, and (d) Schematic bandgap structures of all catalysts.

To clarify the charge carrier separation and transfer efficiency, photoluminescence (PL) spectroscopy was conducted to characterize each sample. Generally, lower PL intensity demonstrated lower recombination of photo-generated electron-hole pairs [72]. With the recombination rate declining, the generation yield of reactive species increased and thus the activity was enhanced accordingly. As shown in Fig. 14a, the PL emission peak intensity for the BiOBr-PVP composites were obviously weakened compared with pristine BiOBr, implying that the recombination of photoinduced electron-hole pairs was efficiently suppressed and thus charge transfer efficiency was increased.

To further verify the above charge carrier mobility, electrochemical impedance spectroscopy (EIS) (Fig.14b) and photocurrent response (Fig.14c) were measured. As shown by EIS Nyquist plots, all catalysts exhibited semi-circular impedance arc radii, and the electrical resistance of BiOBr-PVP composites were much smaller than pure BiOBr, illustrating the positive effect of PVP in the separation of electron-hole pairs and light-harvesting. As expected, B-0.05 composite still exhibited the smallest semicircular radius, indicating fast charge transfer from BiOBr-PVP to the solid/liquid interface and consumption by surface reactions. In addition, for the photocurrent response, BiOBr-PVP composites displayed higher intensity in comparison with pristine BiOBr, and B-0.05 showed the highest intensity, indicating that the combination of PVP with BiOBr catalyst not only boosts the charge carrier separation but also promotes release and transfer carrier. The reduction of charge-migration resistance and enhancement of photocurrent response could effectively improve the quantum yield and then increase photocatalytic activity [73], achieving a synergistic effect between the PVP capping agent and the BiOBr semiconductor.

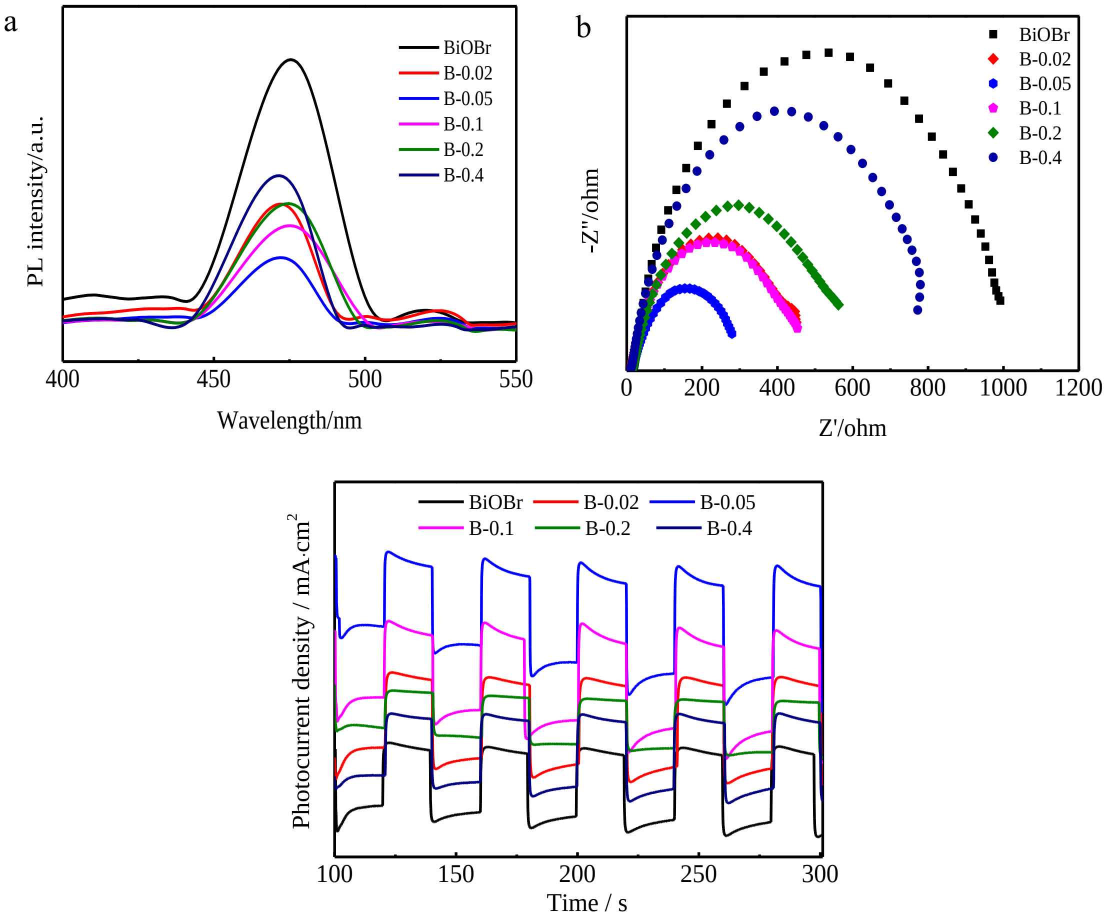

Fig. 14. (a) Photoluminescence spectra, (b) Electrochemical impedance spectra, (c) Photocurrent response of all catalysts

To verify the radical species generated by B-0.05 and gain deeper insight into the photocatalytic process, the BQ, IPA and TEOA were chosen as scavengers for •O_2^-, •OH and h$^+$, respectively [74]. As depicted in Fig. 15a, the introduction of BQ and TEOA significantly decreased the catalytic efficiency, with inhibition of 56.8 and 89% for RhB degradation. This result indicated that holes (h$^+$) and hydroxyl radicals (•OH) played essential roles in the catalytic process. In the presence of IPA, the removal rate of RhB only reduces to 78.6% in 40 min, suggesting the minor role of •OH in RhB photodegradation. To further investigate the function of •OH in photocatalysis using the B-0.05 composite, the IPA was added and the results in compared with other catalysts without addition of IPA. As shown in Fig. 15b, no obvious difference in degradation efficiency was found in the presence of •OH scavengers, indicating that •OH in sample B-0.05 is not the main factor in enhancing the catalytic activity. Based on the above results, it can be concluded that $\bullet O_2^-$, •OH and h^+ coexisted in this system. While $\bullet O_2^-$ and h^+ played major roles, •OH played a supporting role, which were closely consistent with the UV-vis and Mott-Schottky analyses.

Combining with the bandgap structure, scavenging experiments and catalytic activity, a plausible schematic diagram was illustrated in Fig. 15c. The bandgap energy (E_g) of BiOBr-PVP composites is gradually decreased by altering the ratio of added PVP to BiOBr, which can be easily excited and generated electron-hole pairs on the surface of catalyst. The photoinduced electrons could further transfer between BiOBr and PVP at the closely-bonded interface, resulting in efficient charge carrier separation and migration. Afterward, the H_2O and OH^- were oxidized into hydroxyl radicals $\bullet OH/OH^-$ (2.38 V) by photogenerated holes [75]. Owing to the more negative CB potential in comparison with the standard reduction potential of $O_2/\bullet O_2^-$ (-0.33 V), the photoexcited e^- can react with O_2 and generate numerous superoxide radicals $\bullet O_2^-$ [76]. All $\bullet O_2^-$, •OH and h^+ can participate in the RhB oxidation process, and improved the catalytic efficiency compared with pure BiOBr. On the other hand, due to the relatively weaker oxidation effect of $\bullet O_2^-$ compared with photogenerated holes, abundant electrons cannot be fully utilized by O_2, resulting in numerous e^- participating in the photocatalytic reduction process and reducing the highly-toxic Cr(VI) to less toxic Cr(III). The corresponding major reactions in the BiOBr-PVP/ hν system were summarized as follows:

$\mathrm{BiOBr} + h\nu \rightarrow e^-(\mathrm{BiOBr}) + h^+(\mathrm{BiOBr})$ (5)

$e^- + O_2 \rightarrow \bullet O_2^-$ (6)

$h^+ + H_2O/OH^- \rightarrow \bullet OH$ (7)

$h^+/\bullet O_2^-/\bullet OH + \mathrm{RhB} \rightarrow$ small molecules (8)

$Cr_2O_7^{2-} + 14H^+ + 3e^- \rightarrow 2Cr^{3+} + 7H_2O$ (9)

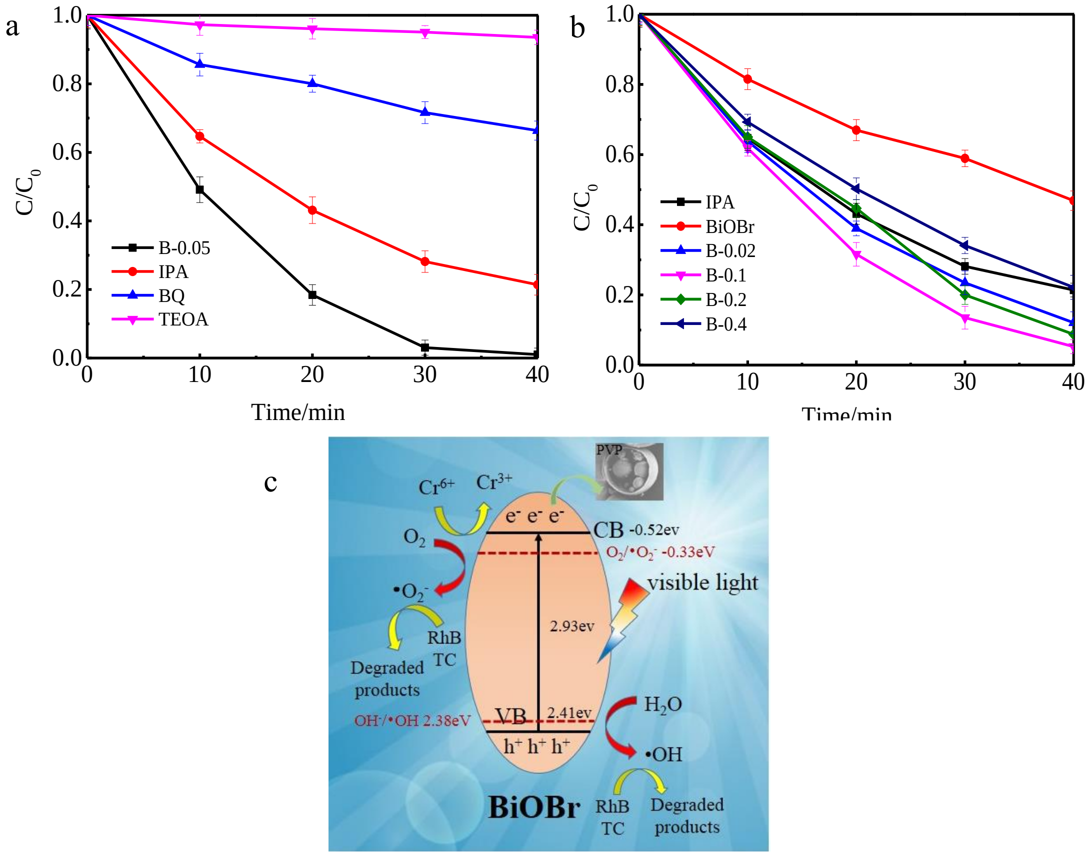

Fig. 15. (a) The RhB photodegradation of B-0.05 with the addition of different scavengers, (b) The photooxidation curves of RhB of B-0.02, B-0.1, B-0.2, B-0.4 and B-0.05 with •OH scavenger, and (c) The possible mechanism of B-0.05 under visible light

4. Conclusions

For the first time a facile precipitation strategy for synthesis of BiOBr-PVP catalysts has been studied. In comparison with pristine BiOBr, BiOBr-PVP composites exhibit lower-energy bandgaps, smaller average particle sizes and more active sites. This led to efficient charge carrier mobility and greater contact area and channels for interaction between the catalyst and pollutants, which exhibited superior photocatalytic activity for organic pollutant oxidation and heavy metal reduction. The appropriate PVP content improved the charge density and decreased the work function, making the charge distribution tend to be more homogenization. The suitable VB-CB band position could simultaneously induce highly active •OH and •O_2^- radicals to participate in the degradation process, even under solar light illumination. Moreover, their excellent stability and recyclability make BiOBr-PVP catalysts promising candidates for further development towards practical environmental remediation media.

Acknowledgments

This work was financially supported by a project grant from the Tokyo Human Resources Fund for City Diplomacy (H29-1).

References

[1] J. Zheng, L. Zhang, Designing 3D magnetic peony flower-like cobalt oxides/g-C_3N_4 dual Z-scheme photocatalyst for remarkably enhanced sunlight driven photocatalytic redox activity, Chem. Eng. J, 369 (2019) 947-956.

[2] P. Mei, H. Wang, H. Guo, N. Zhang, S. Ji, Y. Ma, J. Xu, Y. Li, H. Alsulami, M.S. Alhodaly, T. Hayat, Y. Sun, The enhanced photodegradation of bisphenol A by TiO_2/C_3N_4 composites, Environ Res, 182 (2020) 109090.

[3] Y. Yang, Z. Zheng, D. Zhang, X. Zhang, Response surface methodology directed adsorption of chlorate and chlorite onto MIEX resin and study of chemical properties, Environmental Science: Water Research & Technology, (2020).

[4] Y. Yang, Z. Zheng, W. Ji, J. Xu, X. Zhang, Insights to perfluorooctanoic acid adsorption micro-mechanism over Fe-based metal organic frameworks: Combining computational calculation with response surface methodology, J Hazard Mater, 395 (2020) 122686.

[5] Y. Wang, Y. Wang, L. Yu, R. Wang, X. Zhang, Highly effective microwave-induced catalytic degradation of Bisphenol A in aqueous solution using double-perovskite intercalated montmorillonite nanocomposite, Chem. Eng. J, 390 (2020) 124550.

[6] Y. Wang, L. Yu, R. Wang, Y. Wang, X. Zhang, Reactivity of carbon spheres templated Ce/$LaCo_{0.5}Cu_{0.5}O_3$ in the microwave induced H_2O_2 catalytic degradation of

salicylic acid: Characterization, kinetic and mechanism studies, J Colloid Interface Sci, 574 (2020) 74-86.

[7] J. Chen, X. Zhang, F. Bi, X. Zhang, Y. Yang, Y. Wang, A facile synthesis for uniform tablet-like TiO_2/C derived from Materials of Institut Lavoisier-125(Ti) (MIL-125(Ti)) and their enhanced visible light-driven photodegradation of tetracycline, J Colloid Interface Sci, 571 (2020) 275-284.

[8] X. Zhang, Y. Wang, F. Hou, H. Li, Y. Yang, X. Zhang, Y. Yang, Y. Wang, Effects of Ag loading on structural and photocatalytic properties of flower-like ZnO microspheres, Appl. Surf. Sci, 391 (2017) 476-483.

[9] X. Zhang, Y. Yang, W. Huang, Y. Yang, Y. Wang, C. He, N. Liu, M. Wu, L. Tang, g-C_3N_4/UiO-66 nanohybrids with enhanced photocatalytic activities for the oxidation of dye under visible light irradiation, Materials Research Bulletin, 99 (2018) 349-358.

[10] Y. Wang, J. He, Y. Zhu, H. Zhang, C. Yang, K. Wang, S.-c. Wu, Y.-L. Chueh, W. Jiang, Hierarchical Bi-doped BiOBr microspheres assembled from nanosheets with (001) facet exposed via crystal facet engineering toward highly efficient visible light photocatalysis, Appl. Surf. Sci, 514 (2020) 145927.

[11] K. Wang, Y. Zhang, L. Liu, N. Lu, Z. Zhang, BiOBr nanosheets-decorated TiO_2 nanofibers as hierarchical p–n heterojunctions photocatalysts for pollutant degradation, J. Mater. Sci, 54 (2019) 8426-8435.

[12] Y. Yang, Z. Zheng, M. Yang, J. Chen, C. Li, C. Zhang, X. Zhang, In-situ fabrication of a spherical-shaped Zn-Al hydrotalcite with BiOCl and study on its enhanced photocatalytic mechanism for perfluorooctanoic acid removal performed with a response surface methodology, J Hazard Mater, 399 (2020) 123070.

[13] Y. Sheng, Z. Wei, H. Miao, W. Yao, H. Li, Y. Zhu, Enhanced organic pollutant photodegradation via adsorption/photocatalysis synergy using a 3D g-C_3N_4/TiO_2 free-separation photocatalyst, Chem. Eng. J, 370 (2019) 287-294.

[14] Z. Ai, Y. Shao, B. Chang, L. Zhang, J. Shen, Y. Wu, B. Huang, X. Hao, Rational modulation of p-n homojunction in P-doped g-C_3N_4 decorated with Ti_3C_2 for

photocatalytic overall water splitting, Appl. Cata. B, 259 (2019) 118077.

[15] J. Chen, X. Zhang, X. Shi, F. Bi, Y. Yang, Y. Wang, Synergistic effects of octahedral TiO_2-MIL-101(Cr) with two heterojunctions for enhancing visible-light photocatalytic degradation of liquid tetracycline and gaseous toluene, J Colloid Interface Sci, 579 (2020) 37-49.

[16] S. Son, J.M. Lee, S.-J. Kim, H. Kim, X. Jin, K.K. Wang, M. Kim, J.W. Hwang, W. Choi, Y.-R. Kim, H. Kim, S.-J. Hwang, Understanding the relative efficacies and versatile roles of 2D conductive nanosheets in hybrid-type photocatalyst, Appl. Cata. B, 257 (2019) 117875.

[17] B. Gupta, A.K. Gupta, P.S. Ghosal, C.S. Tiwary, Photo-induced degradation of bio-toxic Ciprofloxacin using the porous 3D hybrid architecture of an atomically thin sulfur-doped g-C_3N_4/ZnO nanosheet, Environ Res, 183 (2020) 109154.

[18] H. Yu, H. Huang, K. Xu, W. Hao, Y. Guo, S. Wang, X. Shen, S. Pan, Y. Zhang, Liquid-Phase Exfoliation into Monolayered BiOBr Nanosheets for Photocatalytic Oxidation and Reduction, ACS Sustainable Chem. Eng, 5 (2017) 10499-10508.

[19] R. Li, J. Liu, X. Zhang, Y. Wang, Y. Wang, C. Zhang, X. Zhang, C. Fan, Iodide-modified $Bi_4O_5Br_2$ photocatalyst with tunable conduction band position for efficient visible-light decontamination of pollutants, Chem. Eng. J, 339 (2018) 42-50.

[20] J. Rashid, A. Abbas, L.C. Chang, A. Iqbal, I.U. Haq, A. Rehman, S.U. Awan, M. Arshad, M. Rafique, M.A. Barakat, Butterfly cluster like lamellar BiOBr/TiO_2 nanocomposite for enhanced sunlight photocatalytic mineralization of aqueous ciprofloxacin, Sci Total Environ, 665 (2019) 668-677.

[21] H. Feng, Z. Xu, L. Wang, Y. Yu, D. Mitchell, D. Cui, X. Xu, J. Shi, T. Sannomiya, Y. Du, W. Hao, S.X. Dou, Modulation of Photocatalytic Properties by Strain in 2D BiOBr Nanosheets, ACS Appl Mater Interfaces, 7 (2015) 27592-27596.

[22] X. Li, J. Xiong, X. Gao, J. Ma, Z. Chen, B. Kang, J. Liu, H. Li, Z. Feng, J. Huang, Novel BP/BiOBr S-scheme nano-heterojunction for enhanced visible-light photocatalytic tetracycline removal and oxygen evolution activity, J Hazard Mater, 387

(2020) 121690.

[23] L. Cao, D. Ma, Z. Zhou, C. Xu, C. Cao, P. Zhao, Q. Huang, Efficient photocatalytic degradation of herbicide glyphosate in water by magnetically separable and recyclable BiOBr/Fe_3O_4 nanocomposites under visible light irradiation, Chem. Eng. J, 368 (2019) 212-222.

[24] D. Zhang, J. Li, Q. Wang, Q. Wu, High {001} facets dominated BiOBr lamellas: facile hydrolysis preparation and selective visible-light photocatalytic activity, J. Mater. Chem. A, 1 (2013) 8622-8629.

[25] S. Qu, Y. Xiong, J. Zhang, Graphene oxide and carbon nanodots co-modified BiOBr nanocomposites with enhanced photocatalytic 4-chlorophenol degradation and mechanism insight, J Colloid Interface Sci, 527 (2018) 78-86.

[26] Z. Li, A. Ivanenko, X. Meng, Z. Zhang, Photocatalytic oxidation of methanol to formaldehyde on bismuth-based semiconductors, J Hazard Mater, 380 (2019) 120822.

[27] C.-J. Chang, P.-Y. Chao, K.-S. Lin, Flower-like BiOBr decorated stainless steel wire-mesh as immobilized photocatalysts for photocatalytic degradation applications, Appl. Surf. Sci, 494 (2019) 492-500.

[28] Q. Fan, X. Chen, F. Chen, J. Tian, C. Yu, C. Liao, Regulating the stability and bandgap structure of BiOBr during thermo-transformation via La doping, Appl. Surf. Sci, 481 (2019) 564-575.

[29] N. Sharma, Z. Pap, S. Garg, K. Hernádi, Hydrothermal synthesis of BiOBr and BiOBr/CNT composites, their photocatalytic activity and the importance of early $Bi_6O_6(OH)_3(NO_3)_3 \cdot 1.5H_2O$ formation, Appl. Surf. Sci, 495 (2019) 143536.

[30] H. Li, J. Shang, Z. Ai, L. Zhang, Efficient Visible Light Nitrogen Fixation with BiOBr Nanosheets of Oxygen Vacancies on the Exposed {001} Facets, J Am Chem Soc, 137 (2015) 6393-6399.

[31] Y. Li, Z. Wang, B. Huang, Y. Dai, X. Zhang, X. Qin, Synthesis of BiOBr-PVP hybrids with enhanced adsorption-photocatalytic properties, Appl. Surf. Sci, 347 (2015) 258-264.

[32] J. Xu, Y. Wang, J. Niu, M. Chen, Facile construction of BiOBr/BiOCOOH p-n heterojunction photocatalysts with improved visible-light-driven photocatalytic performance, Sep. Purif. Technol, 225 (2019) 24-32.

[33] L. Allagui, B. Chouchene, T. Gries, G. Medjahdi, E. Girot, X. Framboisier, A.B.h. Amara, L. Balan, R. Schneider, Core/shell rGO/BiOBr particles with visible photocatalytic activity towards water pollutants, Appl. Surf. Sci, 490 (2019) 580-591.

[34] A.L. Desa, N.H.H. Hairom, D.A.B. Sidik, N. Misdan, N. Yusof, M.K. Ahmad, A.W. Mohammad, A comparative study of ZnO-PVP and ZnO-PEG nanoparticles activity in membrane photocatalytic reactor (MPR) for industrial dye wastewater treatment under different membranes, J. Environ. Chem. Eng, 7 (2019) 103143.

[35] J. Zhou, J. Zhou, Z. Hu, L. Wang, Enhancement of adsorption and visible light photocatalytic activity of the Zn^{2+}-doped BiOBr/PVP modified microspheres for RhB, Mater. Sci. Semicond. Process, 90 (2019) 112-119.

[36] B. Santiago Gonzalez, M.J. Rodriguez, C. Blanco, J. Rivas, M.A. Lopez-Quintela, J.M. Gaspar Martinho, One step synthesis of the smallest photoluminescent and paramagnetic PVP-protected gold atomic clusters, Nano Lett, 10 (2010) 4217-4221.

[37] J. Zhang, M. Zhan, L. Zheng, C. Zhang, G. Liu, J. Sha, S. Liu, S. Tian, FeOCl/POM Heterojunctions with Excellent Fenton Catalytic Performance via Different Mechanisms, Inorg Chem, 58 (2019) 250-258.

[38] G.M. Tomboc, H.S. Jadhav, H. Kim, PVP assisted morphology-controlled synthesis of hierarchical mesoporous $ZnCo_2O_4$ nanoparticles for high-performance pseudocapacitor, Chem. Eng. J, 308 (2017) 202-213.

[39] G.M. Tomboc, F.O. Agyemang, H. Kim, Improved electrocatalytic oxygen evolution reaction properties using PVP modified direct growth Co-based metal oxides electrocatalysts on nickel foam, Electrochimica Acta, 263 (2018) 362-372.

[40] J. Chen, M. Guan, W. Cai, J. Guo, C. Xiao, G. Zhang, The dominant {001} facet-dependent enhanced visible-light photoactivity of ultrathin BiOBr nanosheets, Phys Chem Chem Phys, 16 (2014) 20909-20914.

[41] Y. Guo, Y. Zhang, N. Tian, H. Huang, Homogeneous {001}-BiOBr/Bi Heterojunctions: Facile Controllable Synthesis and Morphology-Dependent Photocatalytic Activity, ACS Sustainable Chem. Eng, 4 (2016) 4003-4012.

[42] K. Dai, G. Dawson, S. Yang, Z. Chen, L. Lu, Large scale preparing carbon nanotube/zinc oxide hybrid and its application for highly reusable photocatalyst, Chem. Eng. J, 191 (2012) 571-578.

[43] L. Ye, J. Liu, Z. Jiang, T. Peng, L. Zan, Facets coupling of BiOBr-g-C_3N_4 composite photocatalyst for enhanced visible-light-driven photocatalytic activity, Appl. Cata. B, 142-143 (2013) 1-7.

[44] X. Xue, R. Chen, H. Chen, Y. Hu, Q. Ding, Z. Liu, L. Ma, G. Zhu, W. Zhang, Q. Yu, J. Liu, J. Ma, Z. Jin, Oxygen Vacancy Engineering Promoted Photocatalytic Ammonia Synthesis on Ultrathin Two-Dimensional Bismuth Oxybromide Nanosheets, Nano Lett, 18 (2018) 7372-7377.

[45] J. Xu, W. Meng, Y. Zhang, L. Li, C. Guo, Photocatalytic degradation of tetrabromobisphenol A by mesoporous BiOBr: Efficacy, products and pathway, Appl. Cata. B, 107 (2011) 355-362.

[46] J. Xi, H. Xia, X. Ning, Z. Zhang, J. Liu, Z. Mu, S. Zhang, P. Du, X. Lu, Carbon-Intercalated 0D/2D Hybrid of Hematite Quantum Dots/Graphitic Carbon Nitride Nanosheets as Superior Catalyst for Advanced Oxidation, Small, 15 (2019) e1902744.

[47] L. Tang, Z.-q. Lv, Y.-c. Xue, L. Xu, W.-h. Qiu, C.-m. Zheng, W.-q. Chen, M.-h. Wu, MIL-53(Fe) incorporated in the lamellar BiOBr: Promoting the visible-light catalytic capability on the degradation of rhodamine B and carbamazepine, Chem. Eng. J, 374 (2019) 975-982.

[48] W. Li, P. Li, Y. Liu, B. Zhang, H. Zhang, W. Geng, Q. Zhang, Efficient Photocatalytic Degradation of Dyes over Hierarchical BiOBr/β-$Co(OH)_2$/PVP Multicomponent Photocatalyst under Visible-Light Irradiation, Chem Cat Chem, 7 (2015) 4163-4172.

[49] X. He, H. Fang, D.J. Gosztola, Z. Jiang, P. Jena, W.N. Wang, Mechanistic Insight

into Photocatalytic Pathways of MIL-100(Fe)/TiO_2 Composites, ACS Appl Mater Interfaces, 11 (2019) 12516-12524.

[50] T. Wang, X. Liu, D. Han, C. Ma, M. Wei, P. Huo, Y. Yan, Biomass derived the V-doped carbon/Bi_2O_3 composite for efficient photocatalysts, Environ Res, 182 (2020) 108998.

[51] B. He, Y. Du, Y. Feng, M. Du, J. Wang, J. Qu, Y. Liu, N. Jiang, J. Wang, X. Sun, Fabrication of novel ternary direct Z-scheme + isotype heterojunction photocatalyst g-C_3N_4/g-C_3N_4/BiOBr with enhanced photocatalytic performance, Appl. Surf. Sci, 506 (2020) 145031.

[52] F. Bi, X. Zhang, J. Chen, Y. Yang, Y. Wang, Excellent catalytic activity and water resistance of UiO-66-supported highly dispersed Pd nanoparticles for toluene catalytic oxidation, Appl. Cata. B, 269 (2020) 118767.

[53] F. Bi, X. Zhang, S. Xiang, Y. Wang, Effect of Pd loading on ZrO_2 support resulting from pyrolysis of UiO-66: Application to CO oxidation, J Colloid Interface Sci, 573 (2020) 11-20.

[54] N. Li, F. Jiao, X. Pan, Y. Ding, J. Feng, X. Bao, Size Effects of ZnO Nanoparticles in Bifunctional Catalysts for Selective Syngas Conversion, ACS Catal, 9 (2018) 960-966.

[55] T. Kanagaraj, S. Thiripuranthagan, Photocatalytic activities of novel $SrTiO_3$ – BiOBr heterojunction catalysts towards the degradation of reactive dyes, Appl. Cata. B, 207 (2017) 218-232.

[56] M.E. Malefane, U. Feleni, P.J. Mafa, A.T. Kuvarega, Fabrication of direct Z-scheme Co_3O_4/BiOI for ibuprofen and trimethoprim degradation under visible light irradiation, Appl. Surf. Sci, 514 (2020) 145940.

[57] H. Zhao, S. Wang, F. He, J. Zhang, L. Chen, P. Dong, Z. Tai, Y. Wang, H. Gao, C. Zhao, Hydroxylated carbon nanotube/carbon nitride nanobelt composites with enhanced photooxidation and H_2 evolution efficiency, Carbon, 150 (2019) 340-348.

[58] J. Li, C. Xiao, K. Wang, Y. Li, G. Zhang, Enhanced Generation of Reactive Oxygen

Species under Visible Light Irradiation by Adjusting the Exposed Facet of FeWO4 Nanosheets To Activate Oxalic Acid for Organic Pollutant Removal and Cr(VI) Reduction, Environ Sci Technol, 53 (2019) 11023-11030.

[59] S. Liu, J. Tian, L. Wang, Y. Luo, X. Sun, One-pot synthesis of CuO nanoflower-decorated reduced graphene oxide and its application to photocatalytic degradation of dyes, Catal. Sci. Technol, 2 (2012) 339-344.

[60] Z. Liang, J. Yang, C. Zhou, Q. Mo, Y. Zhang, Carbon quantum dots modified BiOBr microspheres with enhanced visible light photocatalytic performance, Inorganic Chem Commun, 90 (2018) 97-100.

[61] T. Cai, Y. Liu, L. Wang, W. Dong, H. Chen, W. Zeng, X. Xia, G. Zeng, Activation of persulfate by photoexcited dye for antibiotic degradation: Radical and nonradical reactions, Chem Eng J, 375 (2019) 122070.

[62] C. Yin, S. Zhu, Z. Chen, W. Zhang, J. Gu, D. Zhang, One step fabrication of C-doped $BiVO_4$ with hierarchical structures for a high-performance photocatalyst under visible light irradiation, J. Mater. Chem. A, 1 (2013) 8367-8378.

[63] Z. Niu, Y. Li, Removal and Utilization of Capping Agents in Nanocatalysis, Chemistry of Materials, 26 (2013) 72-83.

[64] H. Chen, H. Luo, Y. Lan, T. Dong, B. Hu, Y. Wang, Removal of tetracycline from aqueous solutions using polyvinylpyrrolidone (PVP-K30) modified nanoscale zero valent iron, J Hazard Mater, 192 (2011) 44-53.

[65] X. Zhang, X. Lv, X. Shi, Y. Yang, Y. Yang, Enhanced hydrophobic UiO-66 (University of Oslo 66) metal-organic framework with high capacity and selectivity for toluene capture from high humid air, J Colloid Interface Sci, 539 (2019) 152-160.

[66] S. Sarkar, R. Das, PVP capped silver nanocubes assisted removal of glyphosate from water-A photoluminescence study, J Hazard Mater, 339 (2017) 54-62.

[67] L. Liu, G. Zheng, F. Yang, Adsorptive removal and oxidation of organic pollutants from water using a novel membrane, Chem. Eng. J, 156 (2010) 553-556.

[68] Z. Jiang, X. Liang, Y. Liu, T. Jing, Z. Wang, X. Zhang, X. Qin, Y. Dai, B. Huang,

Enhancing visible light photocatalytic degradation performance and bactericidal activity of BiOI via ultrathin-layer structure, Appl. Cata. B, 211 (2017) 252-257.

[69] J. Shang, W. Hao, X. Lv, T. Wang, X. Wang, Y. Du, S. Dou, T. Xie, D. Wang, J. Wang, Bismuth Oxybromide with Reasonable Photocatalytic Reduction Activity under Visible Light, ACS Catal, 4 (2014) 954-961.

[70] Z. Jiang, F. Yang, G. Yang, L. Kong, M.O. Jones, T. Xiao, P.P. Edwards, The hydrothermal synthesis of BiOBr flakes for visible-light-responsive photocatalytic degradation of methyl orange, J. Photochem. Photobiol., A, 212 (2010) 8-13.

[71] H. Chen, Y. Liu, T. Cai, W. Dong, L. Tang, X. Xia, L. Wang, T. Li, Boosting Photocatalytic Performance in Mixed-Valence MIL-53(Fe) by Changing Fe(II)/Fe(III) Ratio, ACS Appl Mater Interfaces, 11 (2019) 28791-28800.

[72] L. Ye, X. Jin, C. Liu, C. Ding, H. Xie, K.H. Chu, P.K. Wong, Thickness-ultrathin and bismuth-rich strategies for BiOBr to enhance photoreduction of CO_2 into solar fuels, Appl. Cata. B, 187 (2016) 281-290.

[73] J. Di, J. Xia, M. Ji, B. Wang, S. Yin, Q. Zhang, Z. Chen, H. Li, Advanced photocatalytic performance of graphene-like BN modified BiOBr flower-like materials for the removal of pollutants and mechanism insight, Appl. Cata. B, 183 (2016) 254-262.

[74] H. Huang, X. Han, X. Li, S. Wang, P.K. Chu, Y. Zhang, Fabrication of multiple heterojunctions with tunable visible-light-active photocatalytic reactivity in BiOBr-BiOI full-range composites based on microstructure modulation and band structures, ACS Appl Mater Interfaces, 7 (2015) 482-492.

[75] S. Fu, X. Liu, Y. Yan, L. Li, H. Liu, F. Zhao, J. Zhou, Few-layer WS_2 modified BiOBr nanosheets with enhanced broad-spectrum photocatalytic activity towards various pollutants removal, Sci Total Environ, 694 (2019) 133756.

[76] C. Li, X. Yang, X. Chen, J. Liu, J. Zhang, F. Wang, R. Li, Y. Qu, L. Jing, Construction of a triple sequential junction for efficient separation of photogenerated charges in photocatalysis, Chem Commun, 56 (2019) 197-200.